ISSN 0915-633X

NATIONAL INSTITUTE FOR FUSION SCIENCE

Cubic Interpolated Propagation Scheme for Solving the Hyper-Dimensional Vlasov-Poisson Equation in Phase Space

T. Nakamura and T. Yabe

(Received - Feb. 23, 1999)

NIFS-587 Mar. 1999

RESEARCH REPORT
NIFS Series

NAGOYA, JAPAN

Cubic Interpolated Propagation Scheme for Solving the Hyper-Dimensional Vlasov-Poisson Equation in Phase Space.

Takashi Nakamura and Takashi Yabe
Department of Energy Sciences, Tokyo Institute of Technology
4259 Nagatsuta, Midori-ku, Yokohama 226-8502, Japan

Abstract

A new numerical scheme for solving the hyper-dimensional Vlasov-Poisson equation in phase space is described. At each time step, the distribution function and its first derivatives are advected in phase space by the Cubic Interpolated Propagation (CIP) scheme. Although a cell within grid points is interpolated by a cubic-polynomial, any matrix solutions are not required. The scheme guarantees the exact conservation of the mass. The numerical results show good agreement with the theory. Even if we reduce the number of grid points in v-direction, the scheme still give the stable, accurate and reasonable results with memory storage comparable to particle simulations. Owing to this fact, the scheme has succeeded to be generalized in a straightforward way to deal with the six-dimensional, or full-dimensional problems.

Keywords : Vlasov, Six Dimensions, CIP, Conservative, Grid-Based Algorithm

1. Introduction.

In recent years, various numerical methods have been used for solving the nonlinear Vlasov equation and these methods are roughly divided into two classes. One numerical approach is the particle method that directly follows the trajectories of particles, such as the PIC method (see for review [1,2]). This method has been considered to be quite stable even if only few computational particles are used. Therefore, recent higher dimensional simulations have been performed with this scheme. On the other hand, it is known that this scheme essentially involves some serious disadvantages stemming from statistical numerical noise particularly when detailed structure of distribution is needed for the purpose of transport phenomena like viscosity and heat conduction and for atomic processes.

Another approach is the Eulerian method that uses a hyper-dimensional computational mesh in phase space and the time integration of the distribution function is carried out on each computational mesh point with the help of Fourier – Fourier transform[3], Fourier – Hermite transform[4,5], and splitting method[6]. Because these methods don't involve any source of the statistical noise intrinsic to the particle methods and the profile of the distribution function is stored equally, this numerical approach is more suitable for the simulations in which the particle distribution in a certain velocity region plays an important role [7,8,9]. However, since this method covers all the phase space with grid points, the memory storage and computation time rapidly increases as N^6, N being the grid point needed in one-dimension. With the conventional algorithm, this N has not been sufficiently small leaving the six-dimensional simulation in merely a world of dream. However recent development of numerical algorithm for hyperbolic system has a possibility to bring this dream into reality.

The Cubic Interpolated Propagation (CIP) scheme is a novel unified numerical scheme developed by Yabe et al.[10-13] for the solving hyperbolic equations. The CIP scheme is a low diffusion and stable scheme, and can solve the hyperbolic equations by the 3rd order accuracy both in time and space [14], and this scheme has been successfully applied to various complex fluid flow problems, covering both compressible and incompressible flow, such as laser-induced evaporation [15], shock wave generation, elastic-plastic flow, bubble collapse and so on (see for review [16]). In the CIP scheme first spatial derivatives are introduced as free parameters on each grid point and the time evolution of the derivatives is calculated from the spatial derivatives of a model equation which is consistent with the master equation. Thus, the coefficients of the cubic-polynomial are analytically determined from the physical values and these first derivatives on the neighboring two grid points without any matrix solutions. These facts allow us to easily extend the scheme to hyper-dimensional scheme and solve hyperbolic equations with lower computational effort. Furthermore, the CIP scheme can carry out stable and accurate calculations even if the number of employed computational mesh points is comparatively small. Therefore, it would be very interesting to apply the CIP scheme to the hyper-dimensional Vlasov

equation and examine a possibility of six-dimensional simulation by the present scheme.

This paper presents one possibility to directly simulate the six-dimensional grid system. In section 2, we describe a brief introduction of the CIP scheme and a new numerical technique for calculation of spatial derivatives in hyper-dimensional CIP scheme. Furthermore, we prove that the present CIP scheme exactly conserves total mass in the solution of the Vlasov equation and show a numerical stability and accuracy by some test runs. In section 3, some examples including simulations in two and four-dimensional phase space are represented. In section 4, we actually show a solution of the six-dimensional Vlasov-Poisson equation, and we give a prospect of a simulation in six-dimensional phase space together with conclusion.

2. Numerical Procedure

In this paper, we treat the following normalized one-species collisionless Vlasov-Poisson system;

$$\frac{\partial f}{\partial t} + \mathbf{v}\frac{\partial f}{\partial \mathbf{x}} - \mathbf{E}\frac{\partial f}{\partial \mathbf{v}} = 0, \quad (1)$$

and

$$\frac{\partial}{\partial \mathbf{x}}\mathbf{E} = 1 - \int_{-\infty}^{\infty} f d\mathbf{v}^3, \quad (2)$$

where $f = f(x, y, z, v_x, v_y, v_z)$ and $\mathbf{E} = (E_x, E_y, E_z)$ are the dimensionless distribution function and electric field, respectively. Time is measured in the unit of the inverse plasma frequency $\omega_p^{-1} = (\varepsilon m_e / e^2 n_0)^{1/2}$, length in the unit of the Debye length $\lambda_D = (\varepsilon k_b T_e / e^2 n_0)^{1/2}$ and velocity in the unit of the thermal velocity $v_{th} = \omega_p \lambda_D = (k_b T_e / m_e)^{1/2}$. In this model, an ion background with uniform density (indicated by "1" on the right hand side of Eq.(2)) is assumed.

Since the Vlasov equation (1) is merely advection equation in six-dimensional phase space, obviously it is possible that the CIP scheme is directly applied to the Vlasov - Poisson system.

2.1. Basic Principle of the CIP Scheme.

In this section, the CIP scheme is biefly reviewed by the use of a simple one-dimensional hyperbolic equation:

$$\partial f / \partial t + v \partial f / \partial x = 0. \quad (3)$$

If the velocity v is constant, the theoretical solution of Eq.(3) is obtained by shifting a profile like $f(x, t + \Delta t) = f(x - v\Delta t, t)$. Similarly even if the velocity is not constant, an approximate solution can be given by

$$f(x_i, t + \Delta t) \cong f(x_i - v\Delta t, t), \quad (4)$$

where x_i is the grid point. Equation (4) represents a simple translation of profiles with a velocity v. The initial profile (solid line in Fig.1(a)) moves like a dashed line in a continuous representation. At this time, the solution at grid points is denoted by closed circles and is the same as the exact solution. However, if we eliminate the dashed line as in Fig.1(b), it is hard to imagine the original profile and one may incline to retrieve the original profile like that shown by solid line in Fig.1(c). Thus, numerical diffusion arises when we construct the profile by the linear interpolation even with the exact solution as shown in Fig.1(c). This process is the first-order upwind scheme. On the other hand, if we use quadratic polynomial for interpolation, it suffers from overshooting. This process is the Lax-Wendroff scheme or Leith scheme.

What made this solution worse? For this reason, we have neglected the behavior of the solution inside grid cell and merely follow after the smoothness of the solution. Therefore, we should consider how to incorpolate the real solution into the profile within a grid cell. We propose to approximate the profile as shown below. Let us differentiate Eq.(3) with spatial variable x; then we get

$$\partial(\partial_x f) / \partial t + v\partial(\partial_x f) / \partial x = 0, \quad (5)$$

where $\partial_x f$ abbreviates $\partial f / \partial x$. Equation (5) is the special case of the CIP method in which velocity v is independent of x. As will be shown later, the Vlasov equation is such a simple case. Thus in the simplest case, Eq.(5) coincides with Eq.(3) and represents the propagation of spatial derivative $\partial_x f$ with a velocity v. By this equation, we can trace the time evolution of f and $\partial_x f$ on the basis of Eq.(3). If $\partial_x f$ is predicted as shown by the arrows in Fig.1(d) according to Eq.(5), the profile after one step is limited to a specific profile. It is easy to imagine that by this limitation, the solution becomes very closer to the initial profile.

If two values f and $\partial_x f$ are given at neighboring two grid points, the profile between these points can be described by the cubic polynomial function such as

$$F_i(x) = A1_i X^3 + A2_i X^2 + \partial_x f_i X + f_i, \quad (6)$$

where $X = x - x_i$ The coefficients of Eq. (6), $A1_i$ and $A2_i$ are determined so that the interpolation function and its first derivative is continuous at the both ends:

$$F_i(x_i) = f_i, \quad (\partial F_i / \partial x)_{x=x_i} = \partial_x f_i \qquad (7)$$

$$F_i(x_{iup}) = f_{iup}, \quad (\partial F_i / \partial x)_{x=x_{iup}} = \partial_x f_{iup} \qquad (8)$$

where $iup \equiv i + \mathrm{sgn}(-v_i \Delta t)$ and $\mathrm{sgn}(a)$ means the sign of a. As a result of above simultaneous equations, we have

$$A1_i = (\partial_x f_i + \partial_x f_{iup}) / \Delta x_i^2 + 2(f_i - f_{iup}) / \Delta x_i^3 \qquad (9)$$

$$A2_i = -(2\partial_x f_i + \partial_x f_{iup}) / \Delta x_i - 3(f_i - f_{iup}) / \Delta x_i^2 \qquad (10)$$

where $\Delta x_i \equiv x_{iup} - x_i$. After all, advected profile is given by

$$f_i^{n+1} = F_i(x_i + \xi) = A1_i \xi^3 + A2_i \xi^2 + \partial_x f_i^n \xi + f_i^n, \qquad (11)$$

$$\partial_x f_i^{n+1} = (\partial F_i / \partial x)_{x=x_i - \xi} = 3A1_i \xi^2 + 2A2_i \xi + \partial_x f_i^n, \qquad (12)$$

where $\xi \equiv -v_i \Delta t$ and the superscript "n" indicates the time. In the CIP scheme, matrix solutions for the interpolation like that used in conventional spline is not required at all and the interpolated function can be determined explicitly by using values at neighboring two grid points only. Thus, the scheme can effectively reduce computational cost and suits parallel computations. Here we point out that only Eq. (3) is used to derive Eq. (5) and therefore the gradient $\partial_x f$ in the CIP scheme reflects the physical model written by Eq. (3) differently from one in the spline scheme. Because of this fact, we can expect that interpolated profiles in the CIP scheme are consistent with Eq. (3) to a certain extent.

2.2 Extension of the CIP Scheme to Higher Dimensions.

There exist two methods to extend the one-dimensional CIP to higher dimensions. One is to construct the interpolation profile directly in multi-dimensions[13,17] and to shift the profile in the direction of the velocity vector. However, the cubic polynomial in six-dimensions may not always guarantee the mass conservation that will be discussed later on and may not be worthy for the hard effort of constructing the profile. Another method is to use the technique known as fractional step. We shall use the latter in this paper because of its simplicity and extendability to six dimensions.

For example, let us show two-dimensional case:

$$\partial f / \partial t + v_x \partial f / \partial x + v_y \partial f / \partial y = 0. \qquad (13)$$

where v_x and v_y are the velocities in the x- and y-direction. By the fractional step technique, the solution of Eq.(13) is split into

$$\tilde{f}_{ij}^n = L(x) f_{ij}^n \qquad (14a)$$

$$f_{ij}^{n+1} = L(y) \tilde{f}_{ij}^n \qquad (14b)$$

where $L(\lambda)$ is an operator of any scheme which gives the solution of the equation;

$$\partial f / \partial t + v_\lambda \partial f / \partial \lambda = 0. \qquad (15)$$

Here, we have to pay some attention to the solution of Eqs.(14), because the CIP scheme needs the information of the spatial derivatives. In solving Eq.(14b), (11) and (12) can be directly applied to the y direction with the aid of Eqs. (9) and (10), simply replacing x by y. However, the spatial derivative in the y-direction $\partial_y \tilde{f}_{ij}^n$ is not yet known because in the solution of Eq.(14a) only $\partial_x \tilde{f}_{ij}^n$ is obtained according to Eq.(12). Therefore, some method is required to estimate $\partial_y \tilde{f}_{ij}^n$, although it is automatically calculated in fully multi-dimensional advection without fractional splitting. In order to clarify the computing procedure, let us introduce the "CIP operator" $C(\lambda, \Delta t)$ which means the CIP solution of Eq.(15) by the Eqs. (9), (10), (11) and (12) after Δt time interval. By using this expression, Eq.(13) can be symbolically written as

$$\begin{pmatrix} \tilde{f}_{ij}^n \\ \partial_x \tilde{f}_{ij}^n \end{pmatrix} = C(x, \Delta t) \begin{pmatrix} f_{ij}^n \\ \partial_x f_{ij}^n \end{pmatrix}, \qquad (16)$$

$$\partial_y \tilde{f}_{ij}^n = S(x, y, \Delta t) \partial_x f_{ij}^n, \qquad (17)$$

$$\begin{pmatrix} f_{ij}^{n+1} \\ \partial_y f_{ij}^{n+1} \end{pmatrix} = C(y, \Delta t) \begin{pmatrix} \tilde{f}_{ij}^n \\ \partial_y \tilde{f}_{ij}^n \end{pmatrix}, \qquad (18)$$

$$\partial_x f_{ij}^{n+1} = S(y, x, \Delta t) \partial_y \tilde{f}_{ij}^n, \qquad (19)$$

where $S(\alpha, \beta, \Delta t)$ represents an operator which gives the solution of the equation

$$\frac{\partial}{\partial t}(\partial_\beta f) = -\frac{\partial}{\partial \beta}(v_\alpha \partial_\alpha f) \qquad (20a)$$

which is derived from Eq.(15) by simply taking its

derivative. To calculate Eq.(20a), many methods can be employed. In the previous paper[11], we applied the simplest one, the first-order upwind scheme to the equation

$$\frac{\partial}{\partial t}(\partial_\beta f)+v_\alpha\frac{\partial}{\partial\alpha}(\partial_\beta f)=-\frac{\partial v_\alpha}{\partial\beta}\cdot\partial_\alpha f \qquad (20b)$$

which is an alternative form of Eq.(20a). However, the result was far from that with the direct multi-dimensional scheme and the deformation was quite large. Here, we propose a new scheme which uses simple centered finite difference approach to Eq.(20a) instead of Eq.(20b), and thus Eqs.(17) and (19) are put into

$$\partial_y\tilde{f}_{ij}^n=\partial_y f_{ij}^n-\Delta t(v_{x,i,j+1}\partial_x\tilde{f}_{i,j+1}^n-v_{x,i,j-1}\partial_x\tilde{f}_{i,j-1}^n+v_{x,i,j+1}\partial_x f_{i,j-1}^n-v_{x,i,j-1}\partial_x f_{i,j-1}^n)/4\Delta y \qquad (21a)$$

and

$$\partial_x f_{ij}^{n+1}=\partial_x\tilde{f}_{ij}^n-\Delta t(v_{y,i+1,j}\partial_x f_{i+1,j}^{n+1}-v_{y,i-1,j}\partial_y f_{i-1,j}^{n+1}+v_{y,i+1,j}\partial_x\tilde{f}_{i+1,j}^n-v_{y,i-1,j}\partial_y\tilde{f}_{i-1,j}^n)/4\Delta x \qquad (21b)$$

As shown in the next section, this method exactly guarantees mass conservation law in phase space.

2.3 Mass Conservation Law.

Here, we shall prove that the present method exactly guarantees the mass conservation law in the solution of the Vlasov equation. Let us use a two dimensional equation represented by Eq.(13) with periodic boundary condition for this purpose. We can assume that the velocities v_x and v_y do not depend on the variable x and y, respectively but v_x can be a function of y for example. This is the characteristic of the Vlasov equation in phase space. After one time step, according to Eqs.(11), (12) and (21), physical variables and it's spatial derivatives are written as

$$\tilde{f}_{ij}^n=Al_{ij}\xi^3+A2_{ij}\xi^2+\partial_x f_{ij}^n\xi+f_{ij}^n, \qquad (22a)$$

$$\partial_x\tilde{f}_{ij}^n=3Al_{ij}\xi^2+2A2_{ij}\xi+\partial_x f_{ij}^n, \qquad (22b)$$

$$\partial_y\tilde{f}_{ij}^n=\partial_y f_{ij}^n-\Delta t(v_{x,i,j+1}\partial_x\tilde{f}_{i,j+1}^n-v_{x,i,j-1}\partial_x\tilde{f}_{i,j-1}^n+v_{x,i,j+1}\partial_x f_{i,j+1}^n-v_{x,i,j-1}\partial_x f_{i,j-1}^n)/4\Delta y \qquad (22c)$$

and

$$f_{ij}^{n+1}=Bl_{ij}\chi^3+B2_{ij}\chi^2+\partial_y\tilde{f}_{ij}^n\chi+\tilde{f}_{ij}^n, \qquad (23a)$$

$$\partial_y f_{ij}^{n+1}=3Bl_{ij}\chi^2+2B2_{ij}\chi+\partial_y\tilde{f}_{ij}^n, \qquad (23b)$$

$$\partial_x f_{ij}^{n+1}=\partial_x\tilde{f}_{ij}^n-\Delta t(v_{y,i+1,j}\partial_x f_{i+1,j}^{n+1}-v_{y,i-1,j}\partial_y f_{i-1,j}^{n+1}+v_{y,i-1,j}\partial_x\tilde{f}_{i+1,j}^{n+1}-v_{y,i-1,j}\partial_y\tilde{f}_{i-1,j}^{n+1})/4\Delta x \qquad (23c)$$

where $\xi=-v_{xij}\Delta t$, $\chi=-v_{yij}\Delta t$ and coefficients Al_{ij}, $A2_{ij}$, Bl_{ij} and $B2_{ij}$ are given by applying Eqs.(9), (10) to x- and y-direction:

$$Al_{ij}=(\partial_x f_{ij}^n+\partial_x f_{iup,j}^n)/\Delta x_i^2+2(f_{ij}^n-f_{iup,j}^n)/\Delta x_i^3 \qquad (24a)$$

$$A2_{ij}=-(2\partial_x f_{ij}^n+\partial_x f_{iup,j}^n)/\Delta x_i-3(f_i^n-f_{iup,j}^n)/\Delta x_i^2 \qquad (24b)$$

$$Bl_{ij}=(\partial_y\tilde{f}_{ij}^n+\partial_y\tilde{f}_{i,jup}^n)/\Delta y_j^2+2(\tilde{f}_{ij}^n-\tilde{f}_{i,jup}^n)/\Delta y_j^3 \qquad (25a)$$

$$B2_{ij}=-(2\partial_y\tilde{f}_{ij}^n+\partial_y\tilde{f}_{i,jup}^n)/\Delta y_j-3(\tilde{f}_i^n-\tilde{f}_{i,jup}^n)/\Delta y_j^2 \qquad (25b)$$

where

$iup=i-\mathrm{sgn}(v_x\Delta t)$, $jup=j-\mathrm{sgn}(v_y\Delta t)$,

$\Delta x_i=x_{iup}-x_i$ and $\Delta y_j=y_{jup}-y_j$.

The mass conservation of the present method can be examined by taking a summation of Eqs.(22) and (23) over the entire computational domain. Since $\sum_i Al_{ij}=2\sum_i\partial_x f_{ij}^n$, $\sum_i A2_{ij}=-3\sum_i\partial_x f_{ij}^n$, $\sum_j Bl_{ij}=2\sum_j\partial_y\tilde{f}_{ij}^n$ and $\sum_j B2_{ij}=-3\sum_j\partial_y\tilde{f}_{ij}^n$, we obtain

$$\sum_{ij}\tilde{f}_{ij}^n=\sum_j(2\hat{\xi}^3-3\hat{\xi}^2+\hat{\xi})\Delta x\sum_i\partial_x f_{ij}^n+\sum_{ij}f_{ij}^n, \qquad (26a)$$

$$\sum_i\partial_x\tilde{f}_{ij}^n=(6\hat{\xi}^2-6\hat{\xi}+1)\sum_i\partial_x f_{ij}^n, \qquad (26b)$$

$$\sum_j\partial_y\tilde{f}_{ij}^n=\sum_j\partial_y f_{ij}^n, \qquad (26c)$$

and

$$\sum_{ij}f_{ij}^{n+1}=\sum_i(2\hat{\chi}^3-3\hat{\chi}^2+\hat{\chi})\Delta y\sum_j\partial_y\tilde{f}_{ij}^n+\sum_{ij}\tilde{f}_{ij}^n, \qquad (27a)$$

$$\sum_i\partial_x f_{ij}^{n+1}=\sum_i\partial_x\tilde{f}_{ij}^n, \qquad (27b)$$

$$\sum_j\partial_y f_{ij}^{n+1}=(6\hat{\chi}^2-6\hat{\chi}+1)\sum_j\partial_y\tilde{f}_{ij}^n, \qquad (27c)$$

where $\hat{\xi}=\xi/\Delta x$, $\hat{\chi}=\chi/\Delta y$. Obviously, if the summations of derivatives satisfy a condition

$$\sum_i\partial_x f_{ij}^n=\sum_j\partial_y\tilde{f}_{ij}^n=0, \qquad (28)$$

Eqs.(26a) and (27a) lead to exact conservation form $\sum_{ij}f_{ij}^{n+1}=\sum_{ij}f_{ij}^n$. Furthermore, as a result of Eqs.(26b), (26c), (27b) and (27c), $\sum_i\partial_x f_{ij}^{n+1}$ and $\sum_j\partial_y\tilde{f}_{ij}^{n+1}$ are rewritten as

$$\sum_i\partial_x f_{ij}^{n+1}=(6\hat{\xi}^2-6\hat{\xi}+1)\sum_i\partial_x f_{ij}^n \qquad (29a)$$

$$\sum_j\partial_y f_{ij}^{n+1}=(6\hat{\chi}^2-6\hat{\chi}+1)\sum_j\partial_y\tilde{f}_{ij}^n=(6\hat{\chi}^2-6\hat{\chi}+1)\sum_j\partial_y f_{ij}^n \qquad (29b)$$

Therefore if a relation

$$\sum_i \partial_x f_{ij}^0 = \sum_j \partial_y f_{ij}^0 = 0 \quad (30)$$

holds for the initial condition of computation, then the condition Eq.(28) is always satisfied according to Eqs.(29) and the total mass is exactly conserved at each time step. The condition (28) must be a discretized expression of the continuity of $f(x,y,t)$,

$$\int \partial_x f(x,y,t)dx = \int \partial_y f(x,y,t)dy = 0. \quad (31)$$

Therefore, the condition (28) is considered to be a reasonable requirement from the view point of physics. If initial values of $\partial_x f$ and $\partial_y f$ are given by

$$\partial_x f_{ij}^0 = (f_{i+1,j}^0 - f_{i-1,j}^0)/2\Delta x \quad \text{and}$$
$$\partial_y f_{ij}^0 = (f_{i,j+1}^0 - f_{i,j-1}^0)/2\Delta y, \quad (32)$$

the condition (28) can be automatically satisfied.

In addition to this, even if Eq.(28) does not hold initially, we can prove that the mass conservation is quickly recovered. If we restrict Δt such that $0 \le \hat{\xi} < 1$ and $0 \le \hat{\chi} < 1$ (which corresponds to $\Delta x > \sup|v_x| \cdot \Delta t$ and $\Delta y > \sup|v_y| \cdot \Delta t$, respectively), a function $\Phi(\alpha) = 6\alpha^2 - 6\alpha + 1$ which appears in Eqs.(29a) and (29b) is always less than unity and the following relations hold;

$$\left|\sum_i \partial_x f_{ij}^{n+m}\right| < \ldots < \left|\sum_i \partial_x f_{ij}^{n+1}\right| < \left|\sum_i \partial_x f_{ij}^{n}\right| \quad (33)$$

and

$$\left|\sum_j \partial_y \tilde{f}_{ij}^{n+m}\right| < \ldots < \left|\sum_j \partial_y \tilde{f}_{ij}^{n+1}\right| < \left|\sum_j \partial_y \tilde{f}_{ij}^{n}\right|. \quad (34)$$

Therefore, even if the condition (28) is broken for initial condition, the summations $\sum_i \partial_x f_{ij}^n$ and $\sum_j \partial_y \tilde{f}_{ij}^n$ rapidly vanish in the course of time and the scheme guarantees conservation of total mass after Eq.(28) is established.

Besides the mass conservation, this scheme can provide quite a symmetrical result even if it uses fractional step. This scheme is tested by the two-dimensional solid body rotation problem called as Zalesak's solid-body problem[18]. Figure 2(a) shows the schematic view of this test problem. The value of f inside the cut-off cylinder is 1.0, while outside $f = 0.0$ and the solid-body rotates with a constant angular velocity $\omega = 2\pi$. The other computational conditions are all the same as those in Zalesak's test run. Figures 2(b) and Fig. 2(c) show profiles after one complete revolution. For comparison, the numerical result of spline interpolation method is also shown. In Fig.2(b), the contour of f is plotted from $f = 0.1$ to $f = 1.2$ with increments of 0.1. In the result of spline scheme, the numerical oscillation and diffusion arise and the severe deformation of the upper part is observed, while the present scheme gives a stable and less diffusive result and restores well the shape of the initial profiles. The present scheme has conserved total mass exactly and the relative error was 10^{-16}. We should also mention the computation time. In the spline method, a tridiagonal matrix must be solved in each direction and this would be disadvantageous to parallel computation, while the CIP method suits parallel computation since the scheme is explicit. In the case of Fig.2, the solution of the tridiagonal matrix is straightforward by the use of Gaussian elimination and is quite fast if the boundary is fixed. Even in this case, the CIP method is twice as fast as the spline method (total computation times of the CIP and spline code by a VT-Alpha PC 500AXP were 38.04s and 76.12s, respectively). For the periodic boundary condition employed in many examples given later, the spline method becomes much slower compared with the CIP method.

2.4 Splitting scheme.

In the CIP scheme, hyper-dimensional advection term is split into a sequence of one-dimensional advections in the each directions. When the distribution function is advected in phase space according to the Vlasov equation, it's well known that the trajectory of particles can be solved in the 2nd order accuracy by using the technique known as the splitting method[6]. The Vlasov equation is split into three steps and this procedure is represented by

$$f^*(\mathbf{x},\mathbf{v}) = f^n(\mathbf{x} - \mathbf{v}\Delta t/2, \mathbf{v}) \quad (35)$$
$$f^{**}(\mathbf{x},\mathbf{v}) = f^*(\mathbf{x}, \mathbf{v} + \mathbf{E}^*(\mathbf{x})\Delta t) \quad (36)$$
$$f^{n+1}(\mathbf{x},\mathbf{v}) = f^{**}(\mathbf{x} - \mathbf{v}\Delta t/2, \mathbf{v}) \quad (37)$$

At the first step, the distribution function is advected in the spatial direction for a half time interval $\Delta t/2$. At the next step, the electrical field $\mathbf{E}^*$ is solved according to the Poisson equation using the value f^* of previous step and f^* is advected in the velocity direction for a time interval Δt. At the last step, the distribution function f^{**} is advected in the spatial direction for $\Delta t/2$ again. The orders of advections in each step are quite arbitrary. By a sequential

substitution of Eq.(37) and Eq.(36) into Eq.(35), the series of the advections are expressed as

$$f^{n+1}(\mathbf{x},\mathbf{v}) = f^{*}(\mathbf{x}-\mathbf{v}\Delta t/2, \mathbf{v}+\Delta t\mathbf{E}^{*}(\tau)) = f^{n}(\tilde{\mathbf{x}},\tilde{\mathbf{v}}), \quad (38)$$

where $\tau = \mathbf{x} - \mathbf{v}\Delta t/2$. In the above relation, the arguments of the right hand side f^{n},

$$\tilde{\mathbf{x}} = \mathbf{x} - \mathbf{v}\Delta t + \frac{\Delta t^2}{2}\mathbf{E}^{*}(\tau) \quad \text{and}$$
$$\tilde{\mathbf{v}} = \mathbf{v} + \Delta t\mathbf{E}^{*}(\tau), \quad (39)$$

corresponds to a form of the time integration of the particle motion. We introduce $\mathbf{X}(t)$ as a real particle trajectory and then $\mathbf{E}^{*}(\tau)$ can be regarded as an approximation of $\mathbf{E}(\mathbf{X}(t),t)$ with the first order accuracy in time. Therefore, $\tilde{\mathbf{x}}$ and $\tilde{\mathbf{v}}$ are considered to be equal to a particle trajectory with the 2nd order accuracy in time.

3. Numerical Results.

In this section, some numerical results are described below to demonstrate the accuracy and efficiency of the present method. Especially, we should emphasize a merit of the computational cost; required grid points can be suppressed by using the present method. This fact plays a very important role for the solution of the hyper-dimensional phase space. In reality, reducing the grid point by two in one-direction can get rid of $2^7 = 128$ reduction of computational effort in six-dimensional space and time.

3.1 Two - Dimensional Phase Space.

In order to show the numerical features, first we shall treat the simplest case in two dimensional phase space composed of space x and velocity v_x [19]. The Vlasov-Poisson equation, Eqs.(1) and (2) are rewritten as

$$\partial f(x,v_x,t)/\partial t + v_x \partial f(x,v_x,t)/\partial x - E_x(x,t) f(x,v_x,t)/\partial v_x = 0, \quad (40)$$

and

$$\partial E_x/\partial x = 1 - \int f(x,v_x,t)dv_x. \quad (41)$$

We use the Cartesian mesh to represent the x-v phase space with the computational domain $R = \{(x,v_x) \mid 0 \le x < L, \mid v_x \mid \le v_{off}\}$, where L is the spatial periodic length and v_{off} is the cutoff velocity. The number of mesh points used in x and v_x directions is designated by N and $2M$ respectively. The recurrence effect, the Landau damping and the two stream instability are examined.

A. Recurrence effect for the free-streaming case.

The first example is the recurrence effect for the free-streaming equation which is the advection equation in phase space when $E_x = 0$ in Eq.(40):

$$\partial f(x,v_x,t)/\partial t + v_x \partial f(x,v_x,t)/\partial x = 0. \quad (42)$$

The initial condition is

$$f(x,v_x,0) = 1/\sqrt{2\pi}\exp(-v_x^2/2)\cdot A\cos k_x x, \quad (43)$$

where $A = 0.1$, $k_x = 0.5$, $L = 4\pi$, $v_{off} = 4.0$. The solution of the free-streaming equation is given by:

$$f(x,v_x,t) = f(x - v_x t, v_x, 0) \quad (44)$$

According to Eq.(43) and Eq.(44), the electron density $\rho(x,t)$ is obtained by analytically integrating f over v space,

$$\rho(x,t) = \int_{-\infty}^{+\infty} f(x,v_x,t)dv_x = \exp(-k_x^2 t^2) A\cos(k_x x). \quad (45)$$

On the other hand, the density is numerically obtained:

$$\rho(x,t) = \sum_{j=-M}^{M-1} f(x,v_{x,j},t)\Delta v_x = \sum_{j=-M}^{M-1} f(x - v_{x,j}t, v_{x,j}, t=0)\Delta v_x$$
$$= A\Delta v_x \sum_{j=-M}^{M-1} f_0(v_{x,j})\cos(k_x x - (j+\frac{1}{2})\Delta v_x t) \quad (46)$$

Equation (46) is a summation of periodic functions in time and the density is restored to the initial value at the recurrence time $T_R = 2\pi/\Delta v_x k_x$ [6]. Figure 3 shows a computational result with N=16 M=16. The initial condition is recoverd at $t = 39.0$ with the amplitude $A = 0.0990$, which agrees very well with the theoretical value $T_R = 38.95$ and $A = 0.1$. The total mass of the entire computational domain is exactly conserved. Even if the number of mesh points in the x-direction is reduced to $N = 8$, the recurrence effect is accurately realized and the recurrence time is $t = 38.9$. We should note the second equation in Eq.(46) is the same as Eq.(4) and may not be always satisfied in most of numerical algorithms because $x - v_{x,j}t$ is not given at the grid point and thus we need a method to interpolate it. Therefore, the accurate realization of the recurrence is one of the

demonstrations of our method in advection equation.

B. Landau damping.

The second example is the Landau damping. The Initial condition is

$$f(x,v_x,0) = 1/\sqrt{2\pi}\exp(-v_x^2/2)(1+A\cos k_x x) \quad (47)$$

with $A = 0.01, k_x = 0.5, L = 4\pi$ and $v_{off} = 4.0$. In this case, according to Landau's theory, the phase velocity of the electric field is $v_p = 2.8312$ and the trapped particles are located in the tail of the distribution function. Therefore, generally it is hard to solve this problem with such an initial condition by using particle schemes like the PIC scheme.

Figure 4 shows the time evolution of the basic Fourier component $E_{xk}(k_x = 0.5, t)$ of the electric field E_x with N=32, M=16 and $\Delta t = 1/8$. The amplitude of $E_{xk}(0.5,t)$ decays exponentially in time according to the theory of Landau damping and the recurrence effect appears at around $T_R = 48.7$ which is a theoretical recurrence time predicted from the free-streaming case. The damping rate γ and the frequency ω of the oscillation are 0.1553 and 1.4211, respectively and agree very well with the corresponding theoretical values 0.1533 and 1.4156. The total mass and energy are conserved except for the one caused by roundoff errors and the relative errors stay always less than about 10^{-7} and 10^{-6}, respectively.

Secondly, we shall examine the effect of reduction of the mesh points in v-direction. Figure 5 shows a numerical result with M=8, reduced by half of Fig.4. The Landau damping is computed clearly even with such a coarse grid and the obtained numerical values of γ and ω are 0.1669 and 1.4436, respectively. The agreement can be considered to be good enough, especially if one keep in mind that we are using only 16 mesh points to describe the entire shape of the distribution function in v-direction (which corresponds to 48 "particles" per a spatial mesh point as far as storage is concerned.). Figure 6 shows the dependence of the numerically obtained γ and ω values on the mesh conditions in the v-direction. The dotted line and solid line represent the γ and ω, respectively, and the relative error to the theoretical values are plotted in the logarithmic scale against M. While errors increase with decreasing M, the γ and ω have been computed with reasonable accuracy even if extremely few mesh points are employed such as $M < 10$.

C. Strong nonlinear Landau damping.

When the initial amplitude increases, it is turned into the strong nonlinear Landau damping which has been computed by many authors[3,6,19,20]. The initial condition is also given by Eq.(47) but with $A = 0.5$, $k_x = 0.5$, $L = 4\pi$ and $v_{off} = 5.0$. The numerical result is shown in Figs.7, 8 and 9.

Figure 7 shows the time evolution of the first three Fourier modes. Right after the computation started, the higher modes $E_{xk}(1,t)$ and $E_{xk}(1.5,t)$ are excited and reach their first maximum. The basic mode $E_{xk}(0.5,t)$ damps much more rapidly ($\gamma = -0.280$) than $\gamma_{th} = -0.153$ predicted by the linear theory and reaches its first minimum at $t \cong 15.3$ which shows good agreement with other calculations. Until $t \approx 15$, the second and third mode also damp with $\gamma = -0.584$ and $\gamma = -0.991$, respectively which agree well with values calculated by C. Z. Cheng and G. Knorr[6]. After $t \approx 15$ all three modes grow exponentially until $t \cong 40$ and then saturate. After the saturation, the amplitude of the basic mode oscillates slowly with a period $T \cong 19.8$ which agrees well with the particle trapping time $T_{tr} = 20.99$ calculated from the first maximal value of the basic mode at $t \cong 41.2$.

Figure 8 shows the time development of the spatially integrated distribution function $f_v(v_x,t) = \sum_{i=1}^{N} f(x_i,v_x,t)\Delta x$. The frequency of the oscillation of the basic mode is estimated to be $\omega_{el} \cong 1.4$ and the phase velocity of the electrostatic wave is calculated to be $v_{ph} = \omega_{el}/k_x \cong 2.8$. As predicted by the quasilinear theory, a plateau appears around the phase velocity of the electrostatic wave v_{ph} at $t = 5$. At $t \cong 15$ a small bumps are formed at the phase velocities of the modes and cause all of them to grow. After $t \cong 20$, wrinkles appear and grow rapidly on the main body of the distribution function. The wavenumber agree well with $kt/2\pi$ which is considered to be due to the formed filamentation of the distribution function. As waves grow, the hole in the region $2.0 < v_x < 2.5$ becomes deeper until $t \cong 25$. Then it tends to be filled out until the saturation occurs at $t \cong 40$.

Figure 9 shows the contour plots of the distribution function in the region $1.5 < v_x < 5.0$ and only contours for $f < 1\times10^{-1}$ have been drawn. Right after the computation started, particles are accelerated by the electric field and the tail of the distribution function is dragged out until $t \cong 20$.

From $t \cong 25$ to $t \cong 40$, beginning of trapping the accelerated particles and the appearance of formation of the vortex around the phase velocity v_{ph} are exhibited clearly. After $t \cong 40$ until the end, the trapped particles oscillates in the well of the electrostatic wave and the vortex rotates with a period which corresponds to the slow oscillation of the basic mode after the saturation in Figs.7.

The time development of the distribution function shows good agreement with a result by C. Z. Cheng and G. Knorr[6]. We here used $N = 32$, $M = 128$ and $\Delta t = 1/8$. The relative errors of the conservation of the mass and energy stay always less than 1.0×10^{-5} and 2.0×10^{-3}, respectively. These errors stem from the escape of particles through the velocity boundary. We have decreased Δt to $\Delta t = 1/16$ and the same results are obtained. We also have decreased N to $N = 16$ and results are roughly the same as Figs.7 and the total mass is conserved again with the relative error 1.0×10^{-5}. This example demonstrates that the CIP method can save the special grid points as well as the velocity.

D. Two-stream instability.

We consider the symmetric two-stream instability with initial condition

$$f(x, v_x, 0) = 1/\sqrt{2\pi} v_x^2 \exp(-v_x^2/2)(1 - A\cos k_x x) \qquad (48)$$

where $A = 0.05$, $k_x = 0.5$, $L = 4\pi$ and $v_{off} = 5.0$.

First we used N=32, M=128 and Δt=1/8. The results are shown in Figs.10, 11, 12 and 13. Figure 10 shows the time development of distribution function in phase space. At $t \cong 8.5$, trapping and formation of a vortex starts. From $t \cong 8.5$ to $t \cong 17.8$, the instability grows rapidly and a hole structure appears. After $t \cong 18.0$ until the end, trapped particles oscillate in the electric field and the vortex rotates with a period $T \cong 18$. The time evolutions of the first three Fourier modes of the electric field are depicted as solid curves in Fig.11 where explanatory notes $|E1|$, $|E2|$ and $|E3|$ indicate the amplitudes of $E_{xk}(k = 0.5)$, $E_{xk}(k = 1.0)$ and $E_{xk}(k = 1.5)$, respectively. After an initial transient phase, the first mode $E1$ grows exponentially and reaches it's first maximum at $t \cong 18.0$, then saturates and slowly oscillates due to the trapping of particles. Higher two modes $E2$, $E3$ also grow exponentially and oscillate but always remain inferior to the first mode $E1$. In Fig.12, the development of the electric field energy $W_{el} = 1/2 \sum_i |E_x(x_i, t)|^2$ is plotted by the solid curve(a). W_{el} grows rapidly from $t \cong 8.5$ to $t \cong 17.8$ and oscillates with a period of approximately 18. Conservation of the total mass and energy holds with a relative error 2.3×10^{-5} and 4.4×10^{-4}, respectively from beginning to end. Figure 13 shows the time development of the spatially integrated distribution function. The hole near the minimum $v_x = 0$ is filled as time advances and the filling in of the hole stops at $t \cong 15$ around which saturation of $|E1|$ occurs. After saturation wrinkles appear on the body of the distribution function and remain until the end of the computation. This growth of the wrinkles indicates the progress of filamentations of the distribution function.

Then, the mesh points in v-direction were drastically reduced to M=24 and the evolution for the same initial condition were examined. In Fig.11 and 12, The time evolution of the first three modes and the electric field energy are plotted by dotted curves. We should emphasize that the evolution is quite similar to the case with M=128 and particularly the behavior for $t \leq 20$ can not be distinguished even though 5 times smaller numbers of grids are employed. In Fig12, after saturation, the oscillation of W_{el} is attenuated more rapidly and a period of the oscillation decreases by about 8%. However, every modes and W_{el} exhibit the behavior which agree well with the results of M=128. A profile of the distribution function at t=20.0 is shown in Figs.14. A hole structure appears clearly regardless of M and a trapping of particles is shown as a vortex in the hole structure. For comparison, numerical results of the PIC method for the same initial condition with 72 "particles" per a spatial mesh point are shown in Fig.12(dashed curve(c)) and Figs.14(c). Although this number of particles corresponds to twice larger storage than M=24 of the CIP, the electric field energy and the distribution function in the phase space is poorly described and unclear with the PIC method because of the statistical noise of the particles. Therefore, at least as far as the two-dimensional Vlasov equation concerned, we think that the CIP can solve an entire profile of the distribution function more accurately with a lower computational cost.

We should not forget the pioneering preceding works by the spline method. Although the two-stream instability has been simulated by the spline method[6] and has proved to work well, no information on the distribution function were available. Therefore, we made the program based on the spline method and tested. Time evolution of electric fields were similar to the other method and the CIP method. However, as Fig.14(d) shows the distribution is not as good as the CIP method. In order to quantitatively view the behavior, we plot the cross section of distribution function in Fig.15(b) at two points shown by thick lines in Fig.15(a). We have compared several results

with the coarse and fine grids of the CIP, the coarse and fine grids of the spline method and the PIC method of 229,500 particles which corresponds to 100 times larger storage than the CIP method. This figure shows that the distribution of the spline method has large spikes and large negative value, which increase with fine grids.

3.2 Four - Dimensional Phase Space.

Nextly, we extend the scheme to the four dimensional phase space that consists of two spatial directions x, y and its velocity directions v_x, v_y (Appendix A). According to Eq.(1), the four dimensional Vlasov - Poisson equation is rewritten:

$$\begin{aligned}&\partial f(x,y,v_x,v_y,t)/\partial t + v_x \partial f(x,y,v_x,v_y,t)/\partial x \\ &\quad + v_y \partial f(x,y,v_x,v_y,t)/\partial y \\ &\quad - E_x(x,y,t) f(x,y,v_x,v_y,t)/\partial v_x \\ &\quad - E_y(x,y,t) f(x,y,v_x,v_y,t)/\partial v_y = 0\end{aligned} \tag{49}$$

$$\partial E_x/\partial x + \partial E_y/\partial y = 1 - \iint f(x,y,v_x,v_y,t)\,dv_x dv_y \,. \tag{50}$$

We use the Cartesian mesh to represent the four dimensional phase space with the computational domain

$$\begin{aligned}R = \{(x,y,v_x,v_y) \mid 0 \le x < L_x, 0 \le y < L_y, \\ |v_x| \le v_{xoff}, |v_y| \le v_{yoff}\}\end{aligned} \,;$$

where L_x and L_y are the spatial periodic lengths in the x and y directions, respectively, v_{xoff} and v_{yoff} are the cutoff velocities for the v_x and v_y directions, respectively. The number of mesh points used along the directions x, y, v_x and v_y are designated by N_x, N_y, $2M_x$ and $2M_y$, respectively.

E. Recurrence effect for the free-streaming case.

The first example shows the recurrence effect for the four dimensional free-streaming equation, when $E_x = E_y = 0$ in Eq.(49):

$$\begin{aligned}&\partial f(x,y,v_x,v_y,t)/\partial t + v_x \partial f(x,y,v_x,v_y,t)/\partial x \\ &\quad + v_y \partial f(x,y,v_x,v_y,t)/\partial y = 0\end{aligned} \tag{51}$$

The initial condition of the distribution function is given by:

$$f(x,y,v_x,v_y,0) = f_0(v_x,v_y)(A_x \cos k_x x + A_y \cos k_y y), \tag{52}$$

where $A = A_x = A_y = 0.05$, $k = k_x = k_y = 0.5$ and

$$f_0(v_x,v_y) = 1/2\pi \cdot \exp(-v_x^2/2)\exp(-v_y^2/2). \tag{53}$$

The density $\rho(x,y,t)$ can be integrated analytically as an exponential function:

$$\begin{aligned}\rho(x,y,t) &= \iint f(x,y,v_x,v_y,t)\,dv_x dv_y \\ &= e^{-k^2t^2/2}(A_x \cos k_x x + A_y \cos k_y y)\end{aligned}, \tag{54}$$

in the same way as the two dimensional case, while $\rho(x_i,y_j,t)$ is numerically given by the summation of the periodic functions in time:

$$\begin{aligned}&\rho(x_i,y_j,t) = \\ &\quad \sum_{l=-M_x}^{M_x-1}\sum_{m=-M_y}^{M_y-1} f(x_i - v_{xl}t, y_j - v_{ym}t, v_{xl}, v_{ym}, t=0)\Delta v_x \Delta v_y \\ &= \Delta v_x \Delta v_y \sum_{l=-M_x}^{M_x-1}\sum_{m=-M_y}^{M_y-1} f_0(v_{xl},v_{ym})[A_x \cos(k_x x_i - k_x(l+\frac{1}{2})\Delta v_x t) \\ &\quad + A_y \cos(k_y y_j - k_y(m+\frac{1}{2})\Delta v_y t)]\end{aligned} \tag{55}$$

According to Eq.(55), if the k_x and Δv_x are equal to k_y and Δv_y, respectively, the density $\rho(x_i,y_j,t)$ recovers the initial value $\rho(x_i,y_j,0)$ with the recurrence time $T_R = 2\pi/k_x\Delta v_x = 2\pi/k_y\Delta v_y$. We use $L_x = L_y = 4\pi$, $v_{xoff} = v_{yoff} = 4.0$, $N_x = N_y = 16$, $M_x = M_y = 8$ and $\Delta t = 1/8$. In Fig.16, the time evolution of the density is plotted on the logarithmic scale against time, where the solid curve and dotted curve represent the densities at the positions $(x,y) = (0,0)$ and $(L_x/4,0)$, respectively. The recurrence is observed at $t = 23.5$ and $t = 47.125$ which agree very well with the theoretical recurrence time $T_R = 23.56$ and $2T_R = 47.124$, respectively. Even if the numbers of mesh points in the x, y directions are reduced to $N_x = N_y = 8$, the recurrence effect is accurately computed and the recurrence time is obtained as $t = 23.5$. The total mass of the entire computational domain is exactly conserved in any cases. Figure 17 also shows the change of the density at the positions $x = 0, y = 0$ until $t = 8$, where the solid curve represents the numerical result and the dotted curve represents the theoretical value given by Eq.(54). Until the recurrence effect occurs, the densities exponentially decay in time, as predicted by Eq.(54).

F. Landau damping.

The next example is the Landau damping in the four dimensional phase space. The initial condition is set to

$$f(x,y,v_x,v_y,0) = 1/2\pi \cdot f_0(v_x,v_y) \cdot g(x,y) \qquad (56)$$

where $f_0(v_x,v_y)$ is defined in Eq.(53) and various values will be given to $g(x,y)$ which will be discussed later on.

1.First, we consider the case in which the initial condition is given by

$$g(x,y) = (1 + A\cos k_x x \cos k_y y), \qquad (57)$$

where $A = 0.05$, $v_{off} = v_{xoff} = v_{yoff} = 4.0$, $k_x = k_y = 0.5$, hence $L_x = L_y = 4\pi$ and $N_x = N_y = 16$ and $\Delta t = 1/8$. The same result was obtained, even if we chose a smaller Δt, like $\Delta t = 1/16$, instead of $\Delta t = 1/8$. Furthermore even if $N_x = N_y = 8$ is used, the code gives accurate and stable calculations. Hereafter, the Fourier modes of the electric field components $E_x(x,y)$ and $E_y(x,y)$ are represented by $E_{xk}(\alpha,\beta)$ and $E_{yk}(\alpha,\beta)$, respectively, where α and β are wave numbers. For example, the basic modes are represented by $E_{xk}(0.5,0.5)$ and $E_{yk}(0.5,0.5)$ for this initial condition. Because of the symmetry regarding the x and y coordinates in Eq.(57), $E_{xk}(\zeta,\psi)$ and $E_{yk}(\psi,\zeta)$ are predicted to be equal. Actually, this symmetry was verified from the numerical results. Figure 18 (a) shows the exponential decay of the amplitude of $E_{xk}(0.5,0.5)$. Solid curve represents the numerical result with $M_x = M_y = 16$. $E_{xk}(0.5,0.5)$ decays exponentially with $\gamma = -0.39399$ (damping rate of the oscillation) and $\omega = 1.6973$ (frequency of the oscillation) which agree very well with the theoretical values $\gamma = -0.394$ and $\omega = 1.682$. Dotted curve represents the result with $M_x = M_y = 8$. Even though M_x and M_y were greatly reduced, the numerical values of γ and ω have been calculated with reasonable accuracy ($\gamma = -0.4065$, $\omega = 1.71105$). The recurrence appears around the recurrence time $T_R = 23.56$ as predicted from the free-streaming case. In Fig.18 (b), time evolution of the mode $E_{xk}(0.5,0)$ is shown. Right after computation start, $E_{xk}(0.5,0)$ was excited by the basic mode and then $E_{xk}(0.5,0)$ decays exponentially according to the linear theory. However, amplitude of $E_{xk}(0.5,0)$ remains to be much smaller than $E_{xk}(0.5,0.5)$ and the greater part of the electric field energy is due to $E_{xk}(0.5,0.5)$. The theoretical γ and ω for the mode $E_{xk}(0.5,0)$ are predicted as $\gamma = -0.1533$, $\omega = 1.4156$ from the linear theory. In the case with $M_x = M_y = 16$, a computation gives $\gamma = -0.15915$, $\omega = 1.44305$ and the agreement with theoretical values is fairy good. Even in the case with $M_x = M_y = 8$, the behavior of $E_{xk}(0.5,0)$ shown by the dashed line corresponds to the solid curve of finer grid and the numerical values also agree well($\gamma = -0.15984$, $\omega = 1.46875$). The relative errors of the mass and energy conservation are about 1.2×10^{-6} and 2.0×10^{-5}, respectively and the computation has been very stable.

2. Secondly, we consider the case when the two basic modes $E_{xk}(0.5,0)$ and $E_{yk}(0,0.5)$ initially coexist. The initial condition is given by

$$g(x,y) = (1 + A_x\cos k_x x + A_y \cos k_y y), \qquad (58)$$

where $A_x = A_y = 0.05$, $v_{off} = v_{xoff} = v_{yoff} = 4.0$, $k_x = k_y = 0.5$, hence $L_x = L_y = 4\pi$. We use $N_x = N_y = 16$, $M_x = M_y = 16$ and $\Delta t = 1/8$. This case has been computed by M. M. Shoucri and R. R. J. Gagne with same mesh condition[20,21]. As predicted from symmetry of initial condition regarding x and y, $E_{xk}(\zeta,\psi)$ and $E_{yk}(\psi,\zeta)$ remain to be exactly equal for all the time. In Figs.19(a), time evolution of the amplitude of $E_{xk}(0.5,0)$ is plotted in the logarithmic scale against time. Solid curve represents the numerical result for this mesh condition. $E_{xk}(0.5,0)$ decays exponentially with $\gamma = -0.1542$ and $\omega = 1.4133$ which agree very well with the theoretical values $\gamma = -0.1533$ and $\omega = 1.4156$. In Figs.19(b) and Figs.19(c), the time evolution of the higher two modes $E_{xk}(1,0)$ and $E_{xk}(0.5,0.5)$ is shown with the solid curve. Right after the computation started, those modes were excited. However, for all the time, those amplitudes remained by at least two orders of magnitude smaller than the basic mode $E_{xk}(0.5,0)$. Hence. most of the electric field energy is kept in the basic mode $E_{xk}(0.5,0)$.

Therefore both excited modes $E_{xk}(1,0)$ and $E_{xk}(0.5,0.5)$ show the exponential damping as predicted by the linear theory. However, whereas $E_{xk}(0.5,0.5)$ damps roughly with the theoretical damping rate $\gamma = -0.394$, $E_{xk}(1,0)$ damps much slower than the linear theory and the damping rate is about half of the theoretical rate ($\gamma = -0.851$). The time developments of the higher two modes are quite similar to the Shoucri's results[20,21]. The relative errors of the mass and energy conservation are 5.18×10^{-6} and 1.01×10^{-4}, respectively.

The dotted curves, in the Figs.19(a), Fig.19(b) and Fig.19(c), represent the numerical results when we use the mesh; $N_x = N_v = 16$, $M_x = M_y = 8$. Same values are used for other computational parameters. The basic mode $E_{xk}(0.5,0)$ decay exponentially and the numerical values of γ and ω are -0.1602 and 1.4224, respectively which are in very good agreement with the theoretical values. The higher mode $E_{xk}(1,0)$ shows the recurrence effect at $t = 11.78$. However, until the recurrence time, the higher two modes $E_{xk}(1,0)$ and $E_{xk}(0.5,0.5)$ show the behavior similar to the case with $N_x = N_y = 16$, $M_x = M_y = 16$. We have also verified that the almost same results were obtained with the mesh; $N_x = N_y = 8$, $M_x = M_y = 8$.

4. Six-Dimensional Simulation and Conclusion.

In the present work, we proposed a new numerical scheme for the solution of the hyper-dimensional Vlasov equation. The time integration of the distribution function was carried out by a shift of the distribution function in phase space and the hyper-dimensional advection was calculated by the CIP scheme. The CIP scheme solves the advection explicitly and does not require any matrix solution. Therefore, computational cost was reduced and we verified that computation was at least twice as fast as the spline method with single CPU. Furthermore, we developed a new numerical technique for the calculation of the gradients in the multi-dimensional CIP scheme. By adopting this new technique, the scheme came to exactly guarantee the total mass conservation in the solution of the Vlasov equation, and we proved this fact analytically and verified numerically. The modified CIP scheme was used for Zalesak's test run, and solved the problem more stably, accurately and efficiently than the scheme based on the spline interpolation.

The present scheme has been applied to the solution of hyper-dimensional Vlasov-Poisson system, and solved a number of linear and nonlinear problems in two- and four-dimensional phase space. Unlike the particle methods, the scheme provides noiseless numerical results and a fine resolution for the distribution function all over the phase space including very low density regions. The CIP scheme can provide stable and accurate calculation with much fewer "particles" than the PIC method. Furthermore, even though the computational mesh in velocity direction is very coarse, the present scheme can describe a fine structure of the distribution function without numerical errors such as negative regions of the distribution function, and simulate physics clearly. These facts strongly suggest a possibility that the scheme can be applied to more complex calculation in hyper-dimension and a solution of the full-dimensional Vlasov equation. If the computational mesh points in v - direction could be reduced to $16\times16\times16$ by using the CIP scheme, the required computational memory size is about 1G bytes when the mesh points in x-direction is $16\times16\times16$. By the recent computer development, this amount of the computational cost is considered to be within the capacity of personal computers. Actually, we have completed a six-dimensional Vlasov code based on the procedure given in Appendix A. For example, a numerical result of full-dimensional solution is shown in Fig.20. We used only a personal computer for this calculation and the computation time was 6.7 hours. Furthermore, the CIP method suits parallel computation since the scheme is explicit. Therefore, a larger scale simulation can be carried out easily by the supercomputer and the parallel computers. We should note that we can save the computational grid points in the v-direction if we use the polar coordinate for this direction. This will be an interesting future subject.

Acknowledgements

This work was carried out under the collaborating research program at the National Institute for Fusion Science of Japan. The present work has been supported partly by the Software Research Funding Program of the Center for Promotion of Computational Science and Engineering (CCSE) and Advanced Photon Research Center in Japan Atomic Energy Research Institute (JAERI).

Appendix A.

Four dimensional extension of Eqs.(16) - (19) is straightforward. However, because we adopts the splitting method represented by Eqs.(35), (36) and (37), the four-dimensional advection of the distribution function is split into six steps of the one-dimensional advection and carried out by the following sequential calculations;

Step1:

$$f^{step1}(x,y,v_x,v_y) = f^n(x - v_x\Delta t/2, y, v_x, v_y) \quad \text{(a1)}$$

Step2:

$$f^{step2}(x,y,v_x,v_y) = f^{step1}(x, y - v_y\Delta t/2, v_x, v_y) \quad \text{(a2)}$$

Step3:

$$f^{step3}(x,y,v_x,v_y) = f^{step2}(x, y, v_x + E_x^{n+1/2}\Delta t, v_y) \quad \text{(a3)}$$

Step4:

$$f^{step4}(x,y,v_x,v_y) = f^{step3}(x, y, v_x, v_y + E_y^{n+1/2}\Delta t) \quad \text{(a4)}$$

Step5:

$$f^{step5}(x,y,v_x,v_y) = f^{step4}(x, y - v_y\Delta t/2, v_x, v_y) \quad \text{(a5)}$$

Step6:

$$f^{n+1}(x,y,v_x,v_y) = f^{step5}(x - v_x\Delta t/2, y, v_x, v_y) \quad \text{(a6)}$$

where $E_x^{n+1/2}$ and $E_y^{n+1/2}$ are calculated according to the Poisson equation (50) using the value f^{step2}. Therefore, if four dimensional solution is write down it symbolically, it leads

$$\begin{pmatrix} f_{ijkh}^{step1} \\ \partial_x f_{ijkh}^{step1} \end{pmatrix} = C(x,\Delta t/2)\begin{pmatrix} f_{ijkh}^{n} \\ \partial_x f_{ijkh}^{n} \end{pmatrix}, \quad \text{(a7)}$$

$$\partial_\lambda f_{ijkh}^{step1} = S(x,\lambda,\Delta t/2)\partial_x f_{ijkh}^{n} \quad (\lambda = y, v_x, v_y), \quad \text{(a8)}$$

$$\begin{pmatrix} f_{ijkh}^{step2} \\ \partial_y f_{ijkh}^{step2} \end{pmatrix} = C(y,\Delta t/2)\begin{pmatrix} f_{ijkh}^{step1} \\ \partial_y f_{ijkh}^{step1} \end{pmatrix}, \quad \text{(a9)}$$

$$\partial_\lambda f_{ijkh}^{step2} = S(y,\lambda,\Delta t/2)\partial_y f_{ijkh}^{step1} \quad (\lambda = x, v_x, v_y), \quad \text{(a10)}$$

$$\begin{pmatrix} f_{ijkh}^{step3} \\ \partial_{v_x} f_{ijkh}^{step3} \end{pmatrix} = C(v_x,\Delta t)\begin{pmatrix} f_{ijkh}^{step2} \\ \partial_{v_x} f_{ijkh}^{step2} \end{pmatrix}, \quad \text{(a11)}$$

$$\partial_\lambda f_{ijkh}^{step3} = S(v_x,\lambda,\Delta t)\partial_{v_x} f_{ijkh}^{step2} \quad (\lambda = x, y, v_y), \quad \text{(a12)}$$

$$\begin{pmatrix} f_{ijkh}^{step4} \\ \partial_{v_y} f_{ijkh}^{step4} \end{pmatrix} = C(v_y,\Delta t)\begin{pmatrix} f_{ijkh}^{step3} \\ \partial_{v_y} f_{ijkh}^{step3} \end{pmatrix}, \quad \text{(a13)}$$

$$\partial_\lambda f_{ijkh}^{step4} = S(v_y,\lambda,\Delta t)\partial_{v_y} f_{ijkh}^{step3} \quad (\lambda = x, y, v_x), \quad \text{(a14)}$$

$$\begin{pmatrix} f_{ijkh}^{step5} \\ \partial_y f_{ijkh}^{step5} \end{pmatrix} = C(y,\Delta t/2)\begin{pmatrix} f_{ijkh}^{step4} \\ \partial_y f_{ijkh}^{step4} \end{pmatrix}, \quad \text{(a15)}$$

$$\partial_\lambda f_{ijkh}^{step5} = S(y,\lambda,\Delta t/2)\partial_y f_{ijkh}^{step4} \quad (\lambda = x, v_x, v_y), \quad \text{(a16)}$$

$$\begin{pmatrix} f_{ijkh}^{n+1} \\ \partial_x f_{ijkh}^{n+1} \end{pmatrix} = C(x,\Delta t/2)\begin{pmatrix} f_{ijkh}^{step5} \\ \partial_x f_{ijkh}^{step5} \end{pmatrix}, \quad \text{(a17)}$$

$$\partial_\lambda f_{ijkh}^{n+1} = S(x,\lambda,\Delta t/2)\partial_x f_{ijkh}^{step5} \quad (\lambda = y, v_x, v_y), \quad \text{(a18)}$$

where $C(\lambda,\Delta t)$ is a operator which gives the CIP solution of one-dimensional advection equation (15) and $S(\eta,\lambda,\Delta t)$ is a operator which gives the solution of Eq.(20a) (see section 2.2).

In the six-dimensional case, the time integration of the Vlasov equation is also split into the sequential nine solutions of the one-dimensional advection.

Step1:

$$f^{step1}(x,y,z,v_x,v_y,v_z) = f^n(x - v_x\Delta t/2, y, z, v_x, v_y, v_z) \quad \text{(a19)}$$

Step2:

$$f^{step2}(x,y,z,v_x,v_y,v_z) = f^{step1}(x, y - v_y\Delta t/2, z, v_x, v_y, v_z) \quad \text{(a20)}$$

Step3:

$$f^{step3}(x,y,z,v_x,v_y,v_z) = f^{step2}(x, y, z - v_z\Delta t/2, v_x, v_y, v_z) \quad \text{(a21)}$$

Step4:

$$f^{step4}(x,y,z,v_x,v_y,v_z) = f^{step3}(x, y, z, v_x + E_x^{n+1/2}\Delta t, v_y, v_z) \quad \text{(a22)}$$

Step5:

$$f^{step5}(x,y,z,v_x,v_y,v_z) = f^{step4}(x, y, z, v_x, v_y + E_y^{n+1/2}\Delta t, v_z) \quad \text{(a23)}$$

Step6:

$$f^{step6}(x,y,z,v_x,v_y,v_z) = f^{step5}(x, y, z, v_x, v_y, v_z + E_z^{n+1/2}\Delta t) \quad \text{(a24)}$$

Step7:

$$f^{step7}(x,y,z,v_x,v_y,v_z) = f^{step6}(x, y, z - v_z\Delta t/2, v_x, v_y, v_z) \quad \text{(a25)}$$

Step8:

$$f^{step8}(x,y,z,v_x,v_y,v_z) = f^{step7}(x, y - v_y\Delta t/2, z, v_x, v_y, v_z) \quad \text{(a26)}$$

Step9:

$$f^{n+1}(x,y,z,v_x,v_y,v_z) = f^{step8}(x - v_x\Delta t/2, y, z, v_x, v_y, v_z) \quad \text{(a27)}$$

where $E_x^{n+1/2}$, $E_y^{n+1/2}$ and $E_z^{n+1/2}$ are calculated according to the Poisson equation using the value f^{step3}. Therefore, if six-dimensional solution is write down it symbolically, it leads

$$\begin{pmatrix} f_{ijkh}^{step1} \\ \partial_x f_{ijkh}^{step1} \end{pmatrix} = C(x,\Delta t/2)\begin{pmatrix} f_{ijkh}^{n} \\ \partial_x f_{ijkh}^{n} \end{pmatrix}, \quad \text{(a28)}$$

$$\partial_\lambda f_{ijkh}^{step1} = S(x,\lambda,\Delta t/2)\partial_x f_{ijkh}^{n} \qquad (\lambda = y,z,v_x,v_y,v_z) \quad \text{(a29)}$$

$$\begin{pmatrix} f_{ijkh}^{step2} \\ \partial_v f_{ijkh}^{step2} \end{pmatrix} = C(y,\Delta t/2)\begin{pmatrix} f_{ijkh}^{step1} \\ \partial_v f_{ijkh}^{step1} \end{pmatrix}, \quad \text{(a30)}$$

$$\partial_\lambda f_{ijkh}^{step2} = S(y,\lambda,\Delta t/2)\partial_\lambda f_{ijkh}^{step1} \qquad (\lambda = x,z,v_x,v_y,v_z) \quad \text{(a31)}$$

$$\begin{pmatrix} f_{ijkh}^{step3} \\ \partial_z f_{ijkh}^{step3} \end{pmatrix} = C(z,\Delta t/2)\begin{pmatrix} f_{ijkh}^{step2} \\ \partial_z f_{ijkh}^{step2} \end{pmatrix}, \quad \text{(a32)}$$

$$\partial_\lambda f_{ijkh}^{step3} = S(z,\lambda,\Delta t/2)\partial_z f_{ijkh}^{step2} \qquad (\lambda = x,y,v_x,v_y,v_z) \quad \text{(a33)}$$

$$\begin{pmatrix} f_{ijkh}^{step4} \\ \partial_{v_x} f_{ijkh}^{step4} \end{pmatrix} = C(v_x,\Delta t)\begin{pmatrix} f_{ijkh}^{step3} \\ \partial_{v_x} f_{ijkh}^{step3} \end{pmatrix}, \quad \text{(a34)}$$

$$\partial_\lambda f_{ijkh}^{step4} = S(v_x,\lambda,\Delta t)\partial_{v_x} f_{ijkh}^{step3} \qquad (\lambda = x,y,z,v_y,v_z) \quad \text{(a35)}$$

$$\begin{pmatrix} f_{ijkh}^{step5} \\ \partial_{v_y} f_{ijkh}^{step5} \end{pmatrix} = C(v_y,\Delta t)\begin{pmatrix} f_{ijkh}^{step4} \\ \partial_{v_y} f_{ijkh}^{step4} \end{pmatrix}, \quad \text{(a36)}$$

$$\partial_\lambda f_{ijkh}^{step5} = S(v_y,\lambda,\Delta t)\partial_{v_y} f_{ijkh}^{step4} \qquad (\lambda = x,y,z,v_x,v_z) \quad \text{(a37)}$$

$$\begin{pmatrix} f_{ijkh}^{step6} \\ \partial_{v_z} f_{ijkh}^{step6} \end{pmatrix} = C(v_z,\Delta t)\begin{pmatrix} f_{ijkh}^{step5} \\ \partial_{v_z} f_{ijkh}^{step5} \end{pmatrix}, \quad \text{(a38)}$$

$$\partial_\lambda f_{ijkh}^{step6} = S(v_z,\lambda,\Delta t)\partial_{v_z} f_{ijkh}^{step5} \qquad (\lambda = x,y,z,v_x,v_y) \quad \text{(a39)}$$

$$\begin{pmatrix} f_{ijkh}^{step7} \\ \partial_z f_{ijkh}^{step7} \end{pmatrix} = C(z,\Delta t/2)\begin{pmatrix} f_{ijkh}^{step6} \\ \partial_z f_{ijkh}^{step6} \end{pmatrix}, \quad \text{(a40)}$$

$$\partial_\lambda f_{ijkh}^{step7} = S(z,\lambda,\Delta t/2)\partial_z f_{ijkh}^{step6} \qquad (\lambda = x,y,v_x,v_y,v_z) \quad \text{(a41)}$$

$$\begin{pmatrix} f_{ijkh}^{step8} \\ \partial_y f_{ijkh}^{step8} \end{pmatrix} = C(y,\Delta t/2)\begin{pmatrix} f_{ijkh}^{step7} \\ \partial_y f_{ijkh}^{step7} \end{pmatrix}, \quad \text{(a42)}$$

$$\partial_\lambda f_{ijkh}^{step8} = S(y,\lambda,\Delta t/2)\partial_y f_{ijkh}^{step7} \qquad (\lambda = x,z,v_x,v_y,v_z) \quad \text{(a43)}$$

$$\begin{pmatrix} f_{ijkh}^{n+1} \\ \partial_x f_{ijkh}^{n+1} \end{pmatrix} = C(x,\Delta t/2)\begin{pmatrix} f_{ijkh}^{step8} \\ \partial_x f_{ijkh}^{step8} \end{pmatrix}, \quad \text{(a44)}$$

$$\partial_\lambda f_{ijkh}^{n+1} = S(x,\lambda,\Delta t/2)\partial_x f_{ijkh}^{step8} \qquad (\lambda = y,z,v_x,v_y,v_z) \quad \text{(a45)}$$

References.

[1]. R. W. Hockney and J. W. Eastwood, Computer simulation using particles (*MacGraw-Hill international com,* 1981)

[2]. J. Denavit, Numerical simulation of plasmas with periodic smoothing in phase space, *J. Comput Phys.* **9** , 75 (1972) .

[3]. A. J. Klimas, Numerical method based on the Fourier-Fourier tarnsform approach for modeling 1-D electron plasma evolution, *J. Comput Phys.* **50**, 270 (1983).

[4]. G. Joyce, G. Knorr, Numerical integration methods of the Vlasov equation, *J. Comput. Phys.* **8**, 53 (1971) .

[5]. T. Armstrong, D. Montgomery, Numerical study of weakly unstable electron plasma oscillation, *Phys. Fluids* **12**, 2094 (1969).

[6]. C. Z. Cheng, G. Knorr, The Integration of the Vlasov equation in configuration space, *J. Comput. Phys.* **22**, 330 (1976).

[7]. A. Ghizzo, P. Bertrand, M. M. Shoucri, T. W. Johnston, E. Fijalkow, M. R. Feix, A vlasov code for the numerical simulation of stimulated Raman scattering, *J Comput. Phys.***90**, 431 (1990).

[8]. H. Ruhl, P. Mulser, Relativistic Vlasov simulation of intense fs laser pulse-matter interaction, for the numerical simulation of stimulated Raman scattering, *Phys. Letters* **A 205**, 388 (1990).

[9]. A. Bergmann, P. Mulser, Breaking of resonantly excited electron plasma waves, *Phys. Review* **E 47**, 3585 (1993).

[10]. H. Takewaki, A. Nishiguchi, T. Yabe, *J. Comput. Phys.* **61**, 261 (1985).

[11]. H. Takewaki, T. Yabe, The cubic-interpolated pseudo particle (CIP) method: application to nonlinear and multi-dimensional hyperbolic equations, *J. Comput. Phys.* **70**, 355 (1987).

[12]. T. Yabe, T. Aoki, A universal solver for hyperbolic equations by cubic-polynomial interpolation I. One-dimensional solver, *Comput. Phys. Commun.* **66**, 219 (1991).

[13]. T. Yabe, T. Ishikawa, P. Y. Wang, T. Aoki, Y. Kadota, F. Ikeda, A universal solver for hyperbolic equations by cubic-polynomial interpolation II. Two- and three-dimensional solver, *Comput. Phys. Commun.* **66**, 233 (1991).

[14]. T. Aoki, Interpolated differential operator (IDO) scheme for solving partial differential equation, *Comput. Phys. Commun.* (1997) 1-15.

[15]. T. Yabe and F. Xiao, *Nucl. Eng. Des.* **155**, 45 (1995).

[16]. T. Yabe, Unified solver CIP for solid, liquid and gas, *Computational Fluid Dynamics Review 1998, Ed.by M.M.Hafez and K.Oshima (World Scientific Publishers,1998).*

[17]. T. Aoki, *Comput. Fluid Dyn.* **4**, 279 (1995).

[18]. S. T. Zalesak, *J. Comput. Phys.* **31**, 335 (1979).

[19]. T. Utsumi, T. Kunugi, J. Koga, A numrical method for solving the one-dimensional Vlasov-Poisson equation in phase space, *Comput. Phys. Commun.***108**, 159 (1998).

[20]. M, M, Shoucri, R. R. J. Gagne, A multistep technique for the numerical solution of a two-dimensional Vlasov equation, *J. Comput. Phys.***23**, 242 (1977).

[21]. M, M, Shoucri, R. R. J. Gagne, Splitting scheme for the numerical solution of a two-dimensional Vlasov equation, *J Comput. Phys.***27**, 315 (1978).

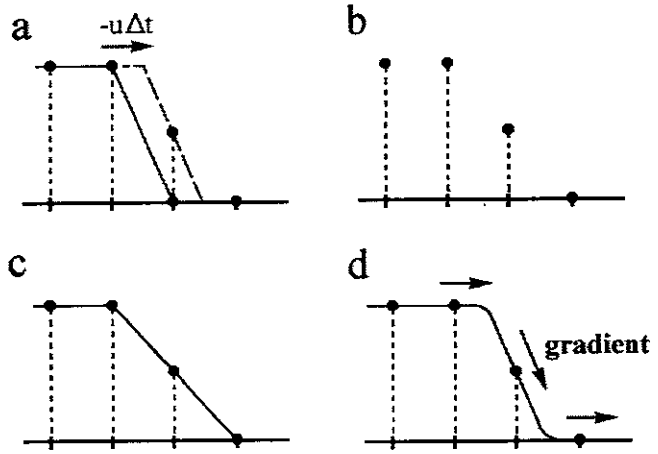

Fig.1 Advection of a profile by the CIP scheme

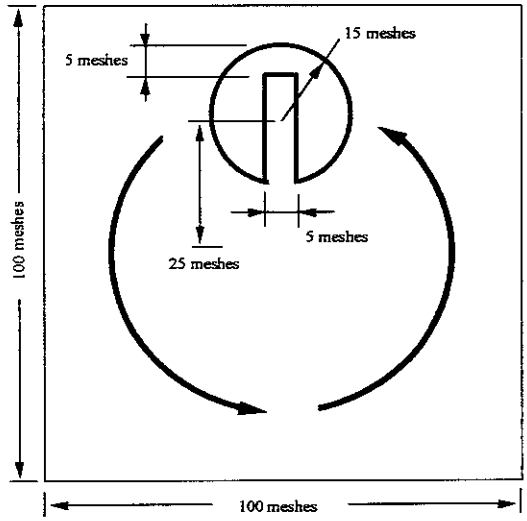

Fig.2(a) Schematic view of Zalesak's solid-body rotation problem. The value of f inside cut-out cylinder is 1.0, while outside $f = 0.0$. The velocities are given by $v_x = -\omega y$ and $v_y = \omega x$, where ω is an angular velocity and $\omega = 2\pi$.

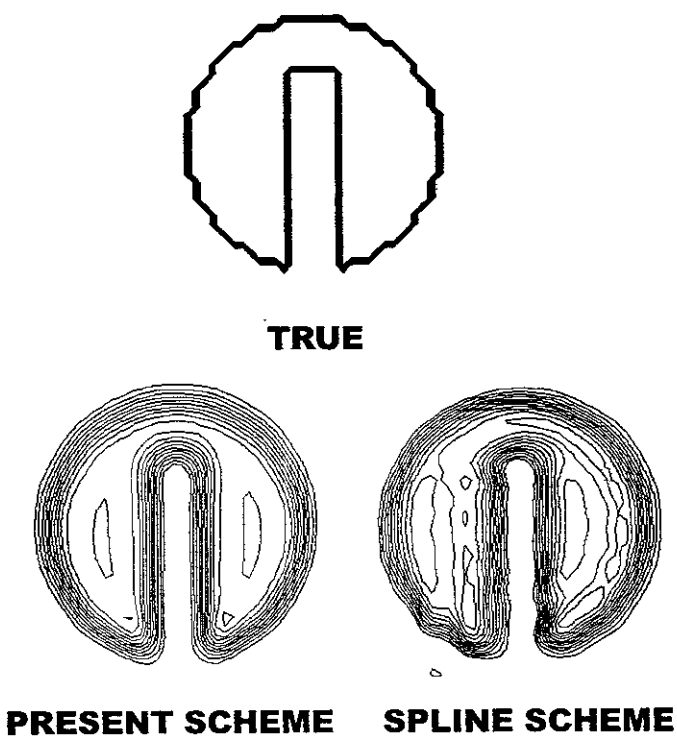

Fig.2(b) Contour plots of the computational results for Zalesak's problem after one complete evolution.

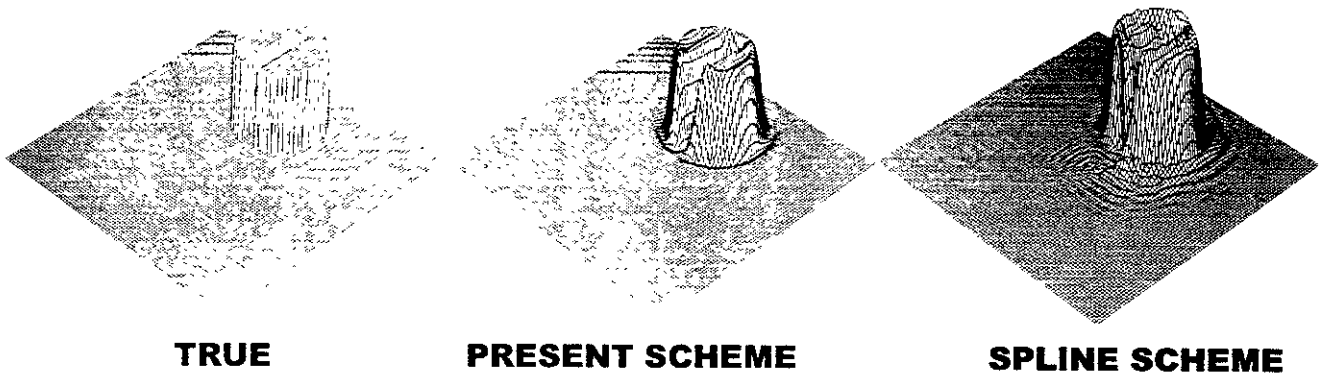

Fig 2(c) Three-dimensional views of the computational results for Zalesak's test problem after one complete evolution.

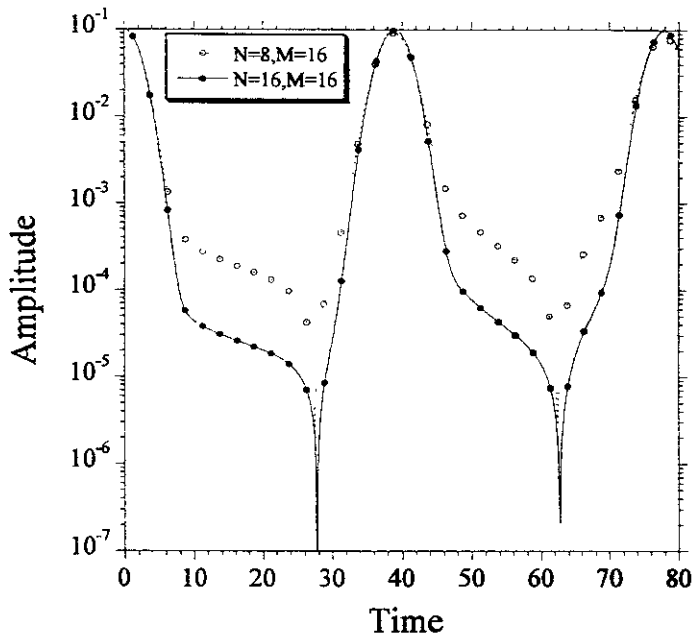

Fig.3 The recurrence effect for the numerical free-streaming solution with $A = 0.1, k_x = 0.5, v_{off} = 5.0$, $M = 16$ and $\Delta t = 1/8$.

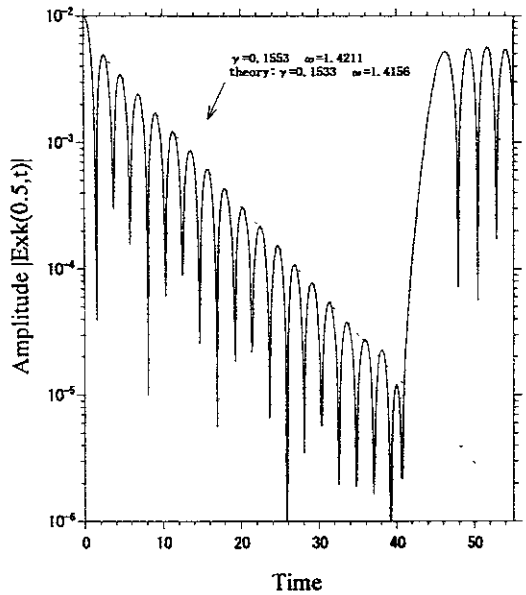

Fig.4 Linear Landau damping with recurrence effect . $A = 0.01, k_x = 0.5, v_{off} = 4.0$, $N = 32, M = 16$ and $\Delta t = 1/8$. The theoretical recurrence time is $T_R = 48.69$.

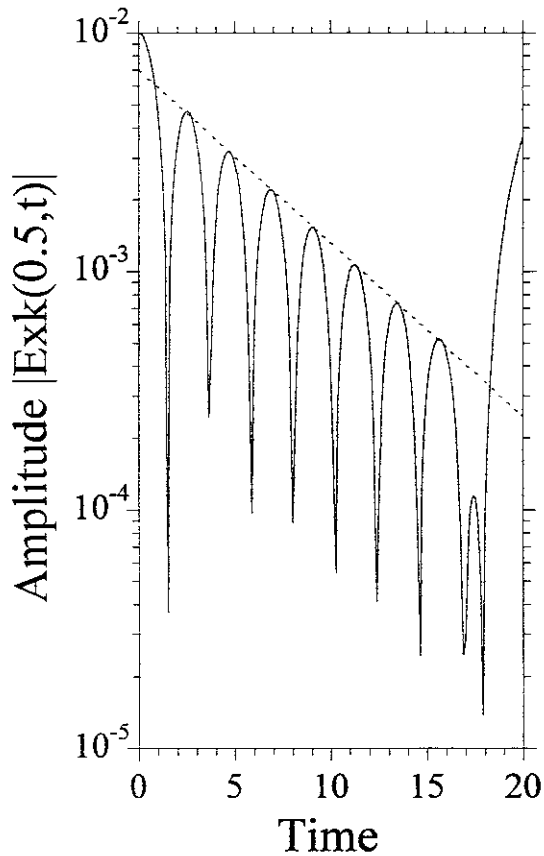

Fig.5 Linear Landau damping with reduced mesh points.The initial condition is the same as Fig.4 and the computation mesh is $N = 32$, $M = 8$ with $k_x = 0.5, v_{off} = 4.0$ and $\Delta t = 1/8$.

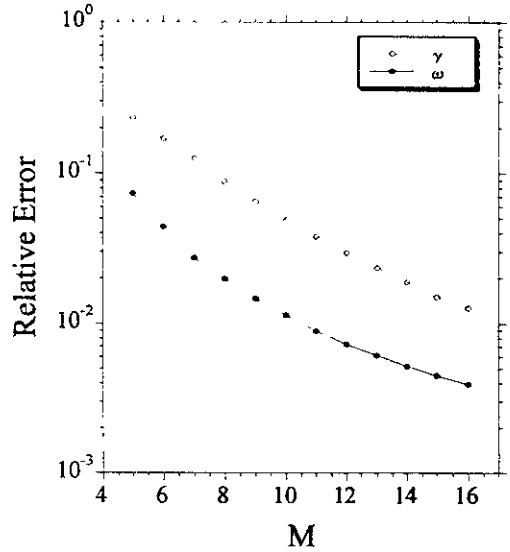

Fig.6 Relative error to the theoretical value. The solid and dashed curves represent the frequency and the damping rate respectively. $A = 0.01, k_x = 0.5, v_{off} = 4.0, N = 32$ and $\Delta t = 1/8$.

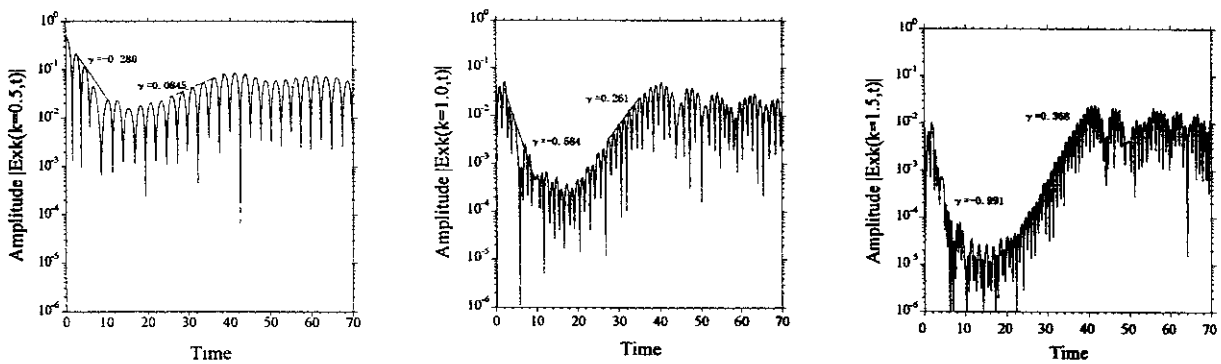

Fig.7 Amplitudes of the first three modes of the electric field for the strong nonlinear Landau damping with $A = 0.5, k_x = 0.5, v_{off} = 5.0, L_x = 4\pi, N = 32, M = 16$ and $\Delta t = 1/8$.

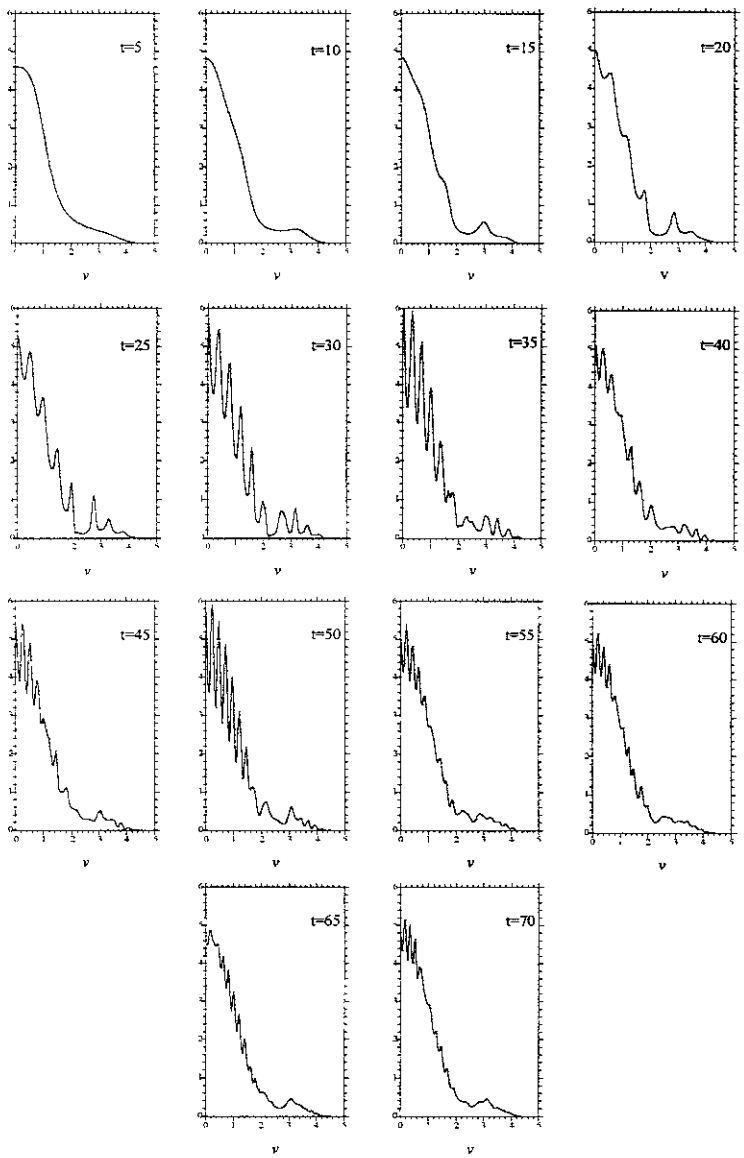

Fig.8 Time development of the spatially integrated distribution function for the strong nonlinear Landau damping.

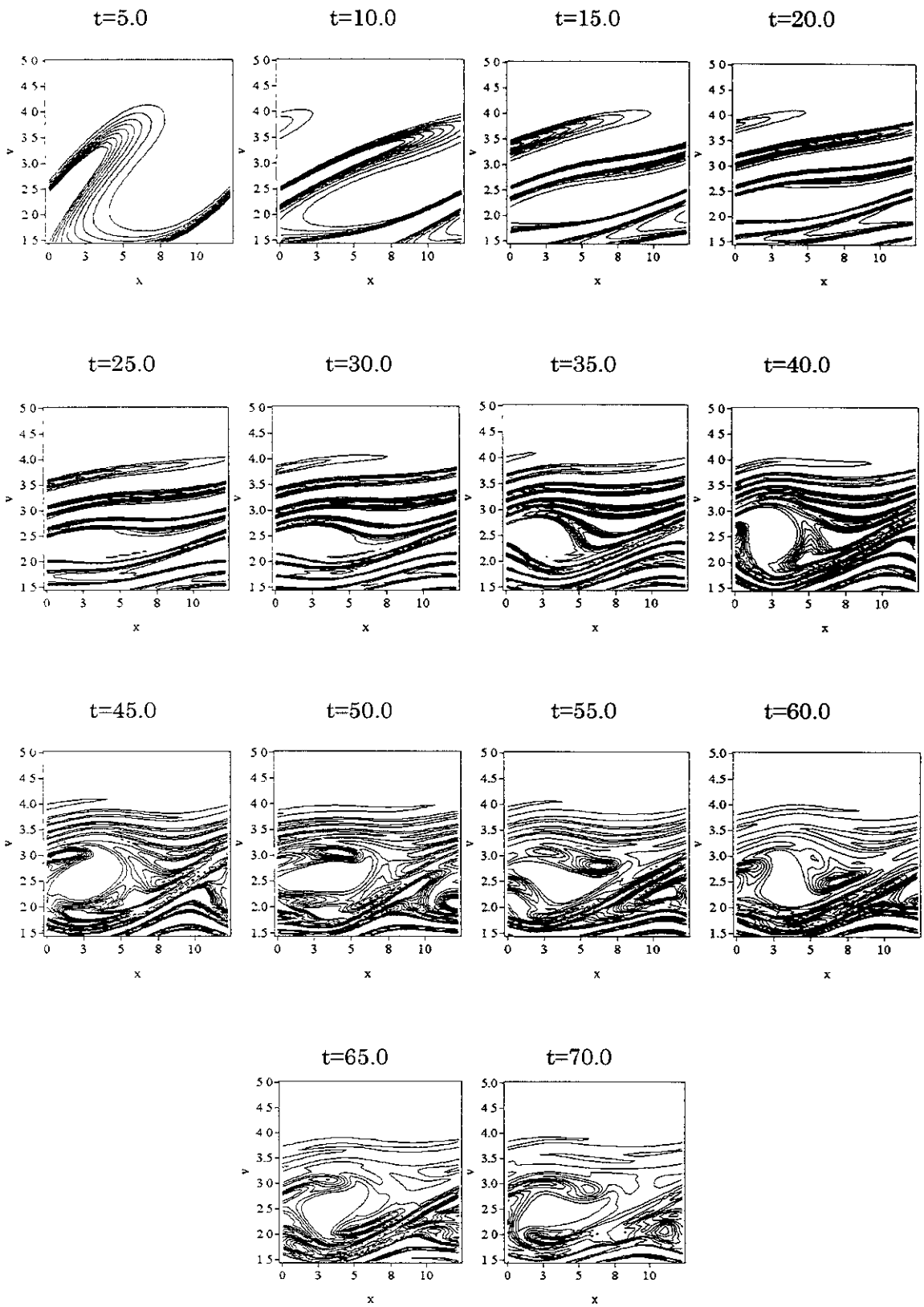

Fig.9 The time development of the distribution function in the strong nonlinear Landau damping.

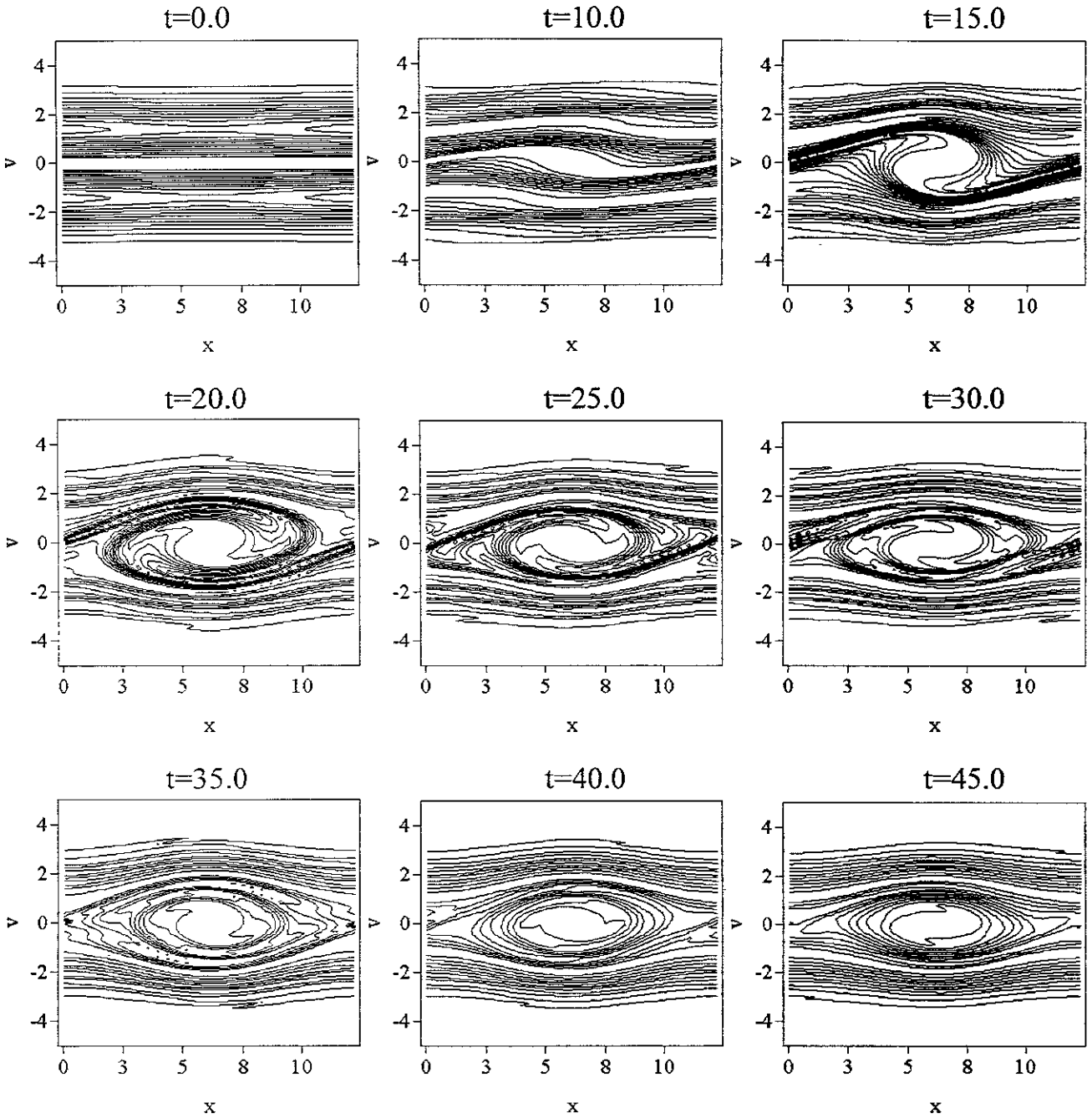

Fig.10 Appearance of a hole structure in the two-stream instability. The initial condition is given by Eq.(48) with $A=0.05$, $k_x=0.5$, $L=4\pi$, $v_{off}=5.0$, N=32, $M=128$ and $\Delta t=1/8$.

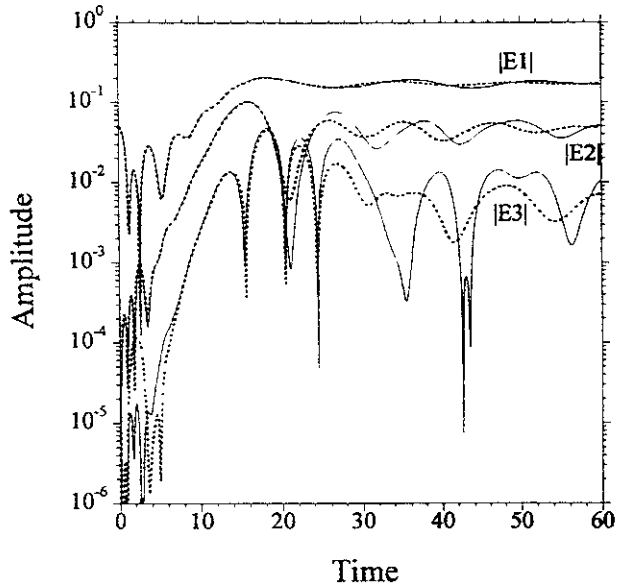

Fig.11 The time evolution of the first three modes for the two-stream instability, where $E1$, $E2$ and $E3$ indicate the Fourier mode $E_{xk}(k=0.5)$, $E_{xk}(k=1)$ and $E_{xk}(k=1.5)$, respectively. The initial condition is given by Eq.(48) with $A=0.05$, $k_x=0.5, L=4\pi, v_{off}=5.0$,N=32 and Δt=1/8. Solid curves and dotted curves represent the numerical results with $M=128$ and $M=24$, respectively.

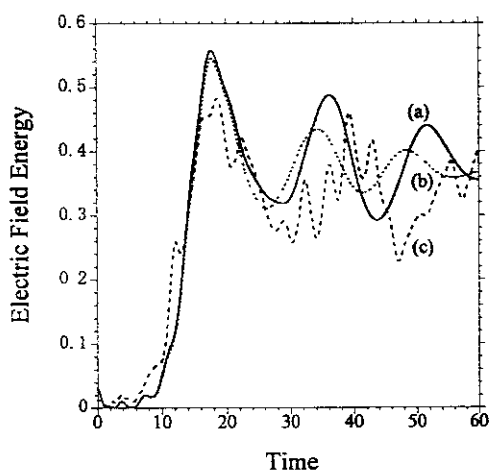

Fig.12 The time evolution of the total electric field energy for the two-stream instability. Solid curve(a) and dotted curve(b) represent the numerical results of the present scheme with $M=128$ and $M=24$, respectively. Dashed curve(c) represents the result of the PIC scheme with 4608 "particles" which corresponds to M=24(curve (b)) as far as storage is concerned.

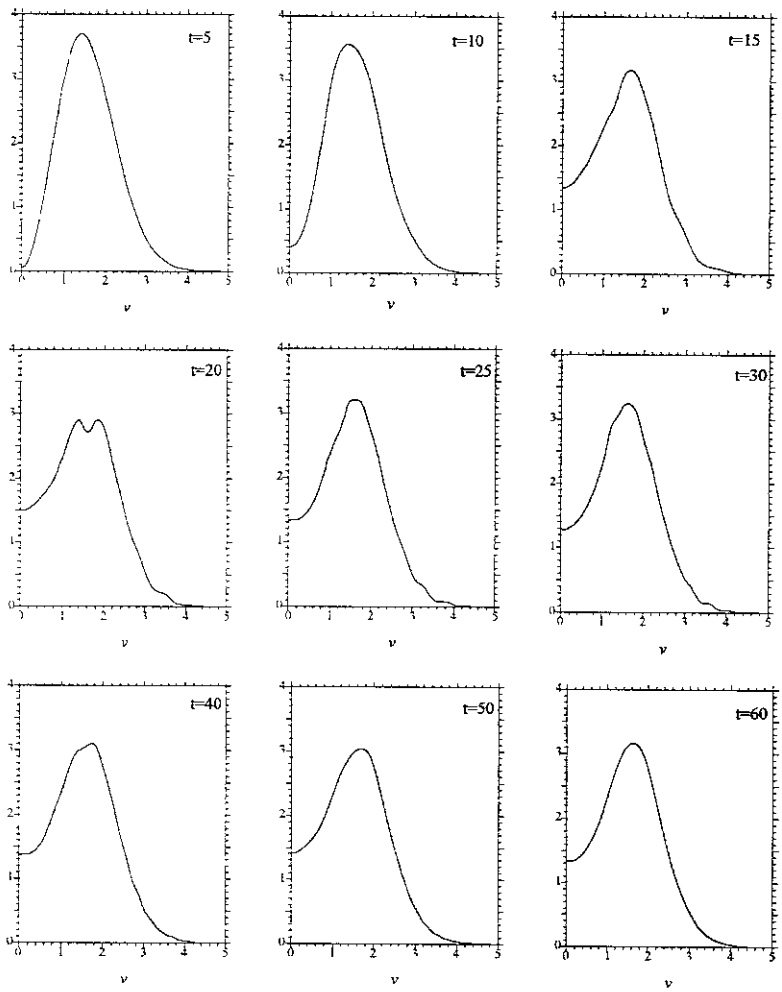

Fig.13 Time development of the spatially integrated dstribution function for two-stream instability.

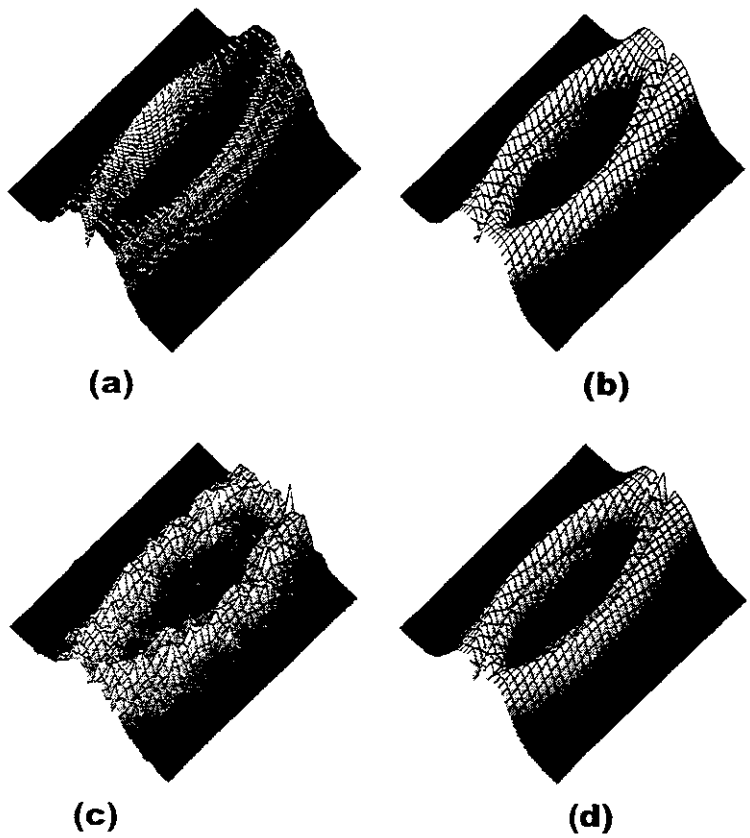

Fig.14. Over-view profile of the distribution function at t=20.0 using (a) CIP (M=128), (b) CIP (M=24), (c) PIC (4608 "particles", correspond to twice larger storage than M=24 of CIP) and (d) spline method (M=24).

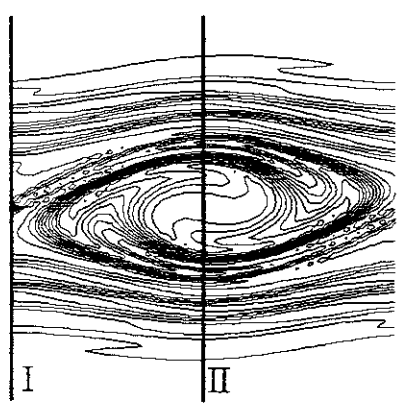

Fig.15(a) The positions of cross sections shown in Fig.15(b). " I " is x=0.0 and " II " is $x=2\pi$.

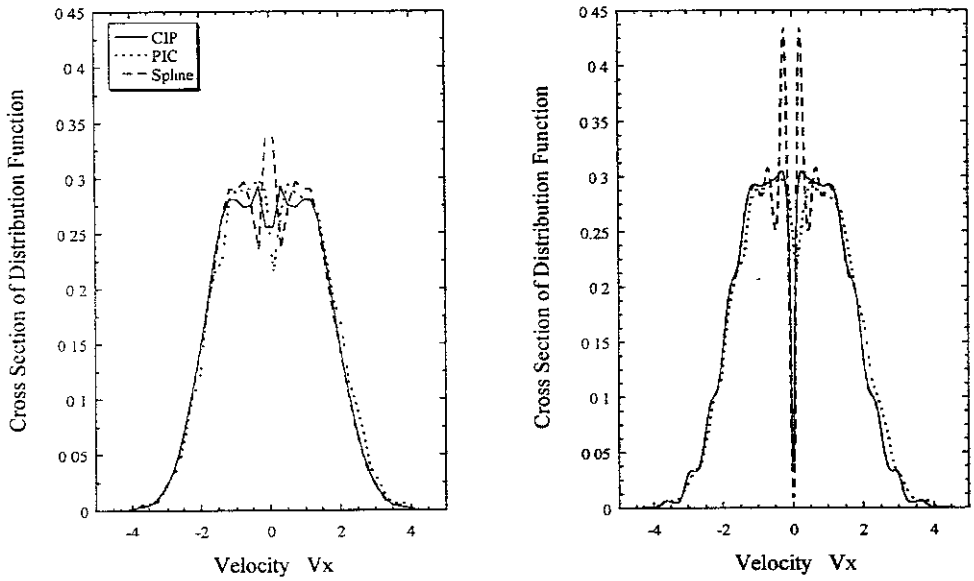

(I-1) (I-2)

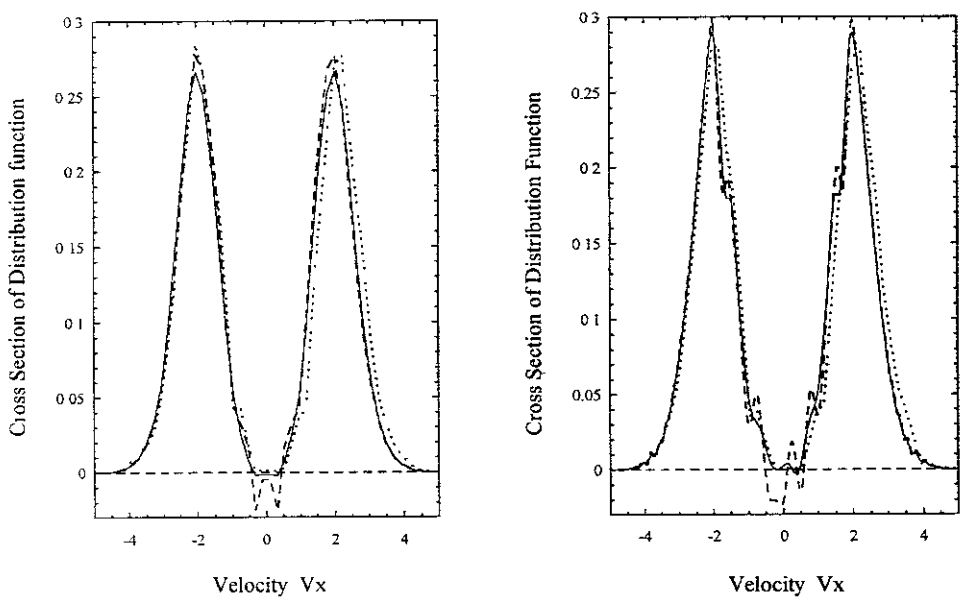

(II-1) (II-2)

Fig.15(b) Cross sections of distribution function vertical to x-axis for two-stream instability. Figure (I-1) and (I-2) are along the line (I) in Fig.15(a) at t=22.5, and Fig.(II-1) and (II-2) are along the line (II) at t=53.75. In each figure, a solid curve shows the result by the CIP, a dashed curve shows the result by the spline method, and a dotted curve shows the result by the PIC. Figure (I-1) and (II-1) are results with $M_x = 24$, and Figure (I-2) and (II-2) are results with $M_x = 128$. We use quite a lot of particles (229,500 particles) in the PIC code to reduce the noise in the distribution function.

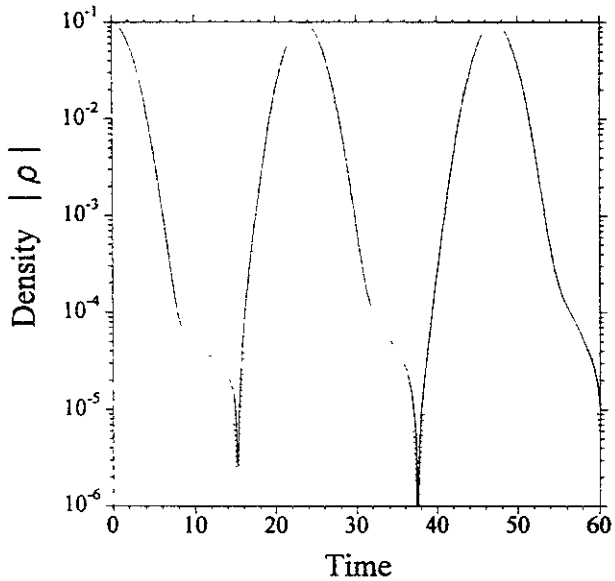

Fig.16 Time evolution of the density at the positions x=0,y=0 (solid curve) and x=Lx/4,y=0 (dotted curve) for the four dimensional free-streaming equation, and for the initial condition in Eq.(52) with $A_x = A_y = 0.05, k_x = k_y = 0.5, L_x = L_y = 4\pi, v_{xoff} = v_{yoff} = 4.0, N = 16$ and $M = 8$.

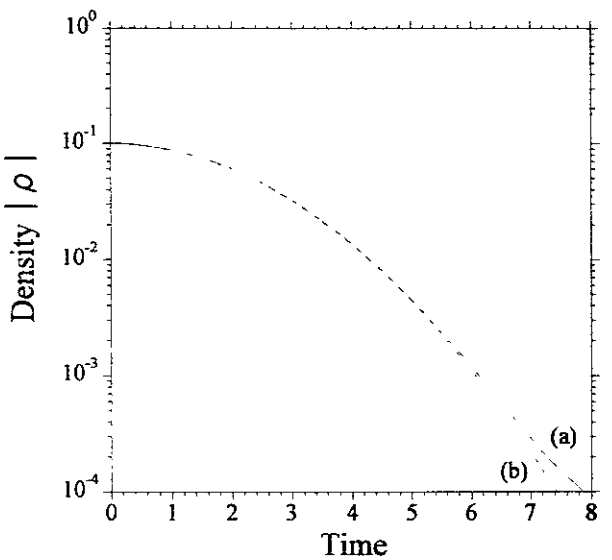

Fig.17 Time evolution of the density at the position x=0,y=0 for the four dimensional free-streaming equation. A solid curve(a) and dashed curve(b) represent the computational result and theoretical result in Eq.(54), respectively.

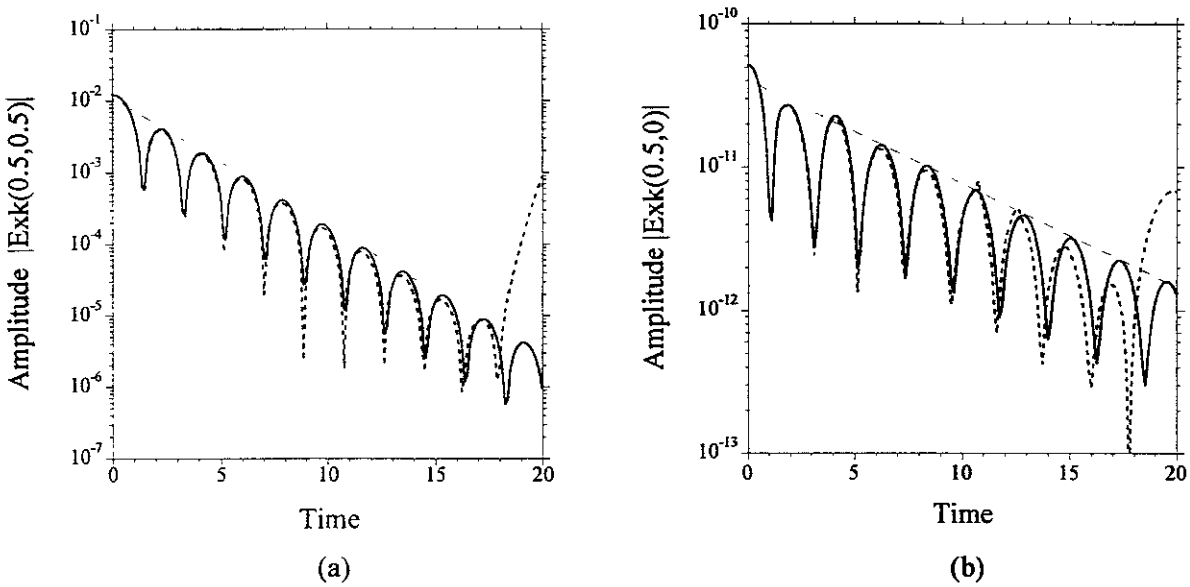

Figs.18 The Landau damping for the four-dimensional Vlasov equation as discussed in the case **F-1**. Figure (a) and (b) show the time development of the basic Fourier mode $E_{xk}(0.5,0.5)$ and the excited mode $E_{xk}(0.5,0)$, respectively. The initial condition is given by Eq.(57) and the parameters are $A=0.05$, $v_{off}=v_{xoff}=v_{yoff}=4.0$, $k_x=k_y=0.5$, $L_x=L_y=4\pi$, $N_x=N_y=16$ and $\Delta t=1/8$. In each plot, the solid curve represents the numerical result with $M_x=M_y=16$ and the dotted curve represents value with $M_x=M_y=8$.

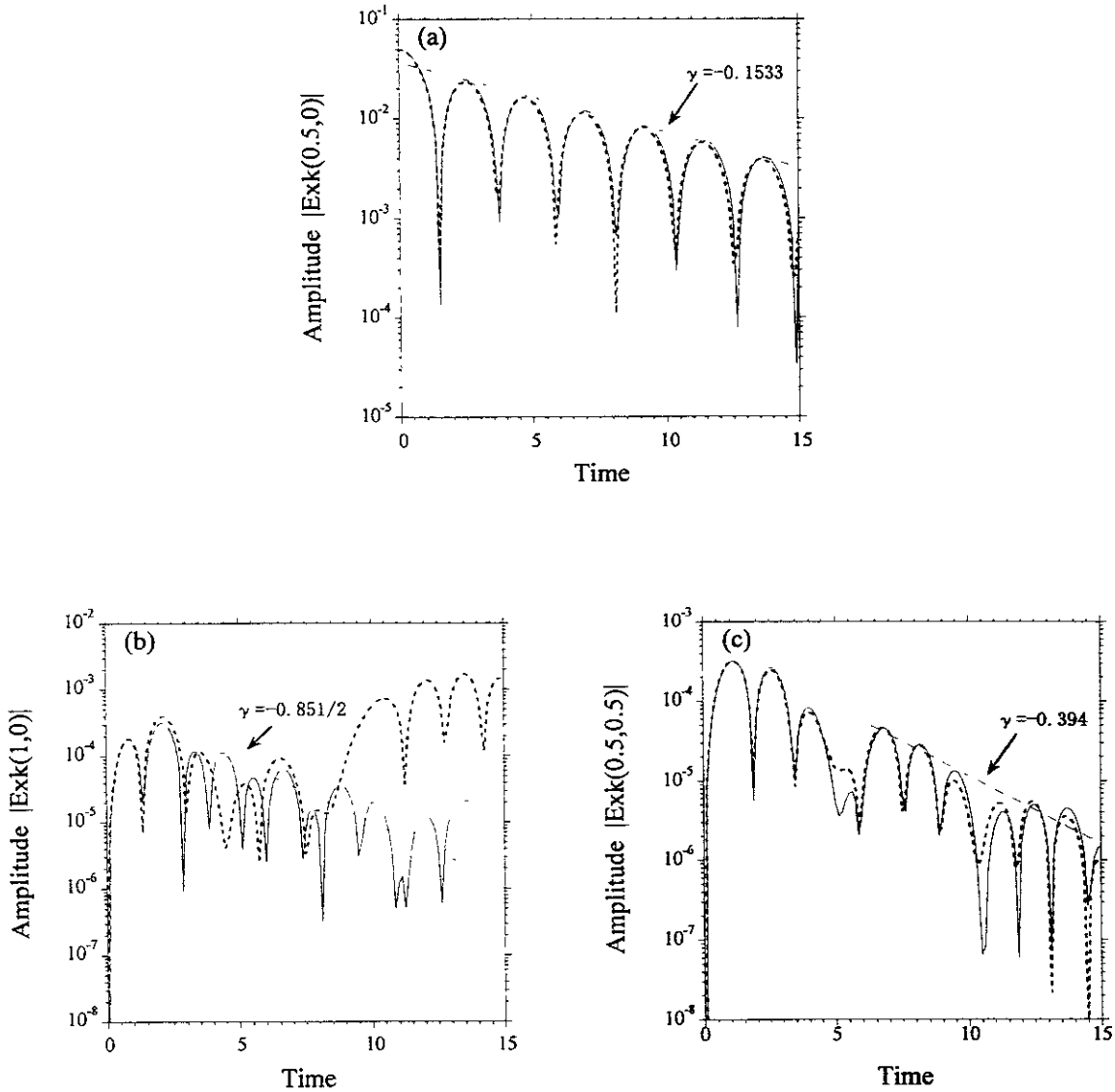

Figs.19 The Landau damping for the solution of the four-dimensional Vlasov equation in the case F2. The time developments of the basic mode $E_{xk}(0.5,0)$ and excited modes $E_{xk}(1,0)$, $E_{xk}(0.5,0.5)$ are plotted in (a), (b) and (c), respectively. In each plot, the solid curve and the dotted curve represent the numerical results for the case with $M_x = M_y = 16$ and $M_x = M_y = 8$, respectively.

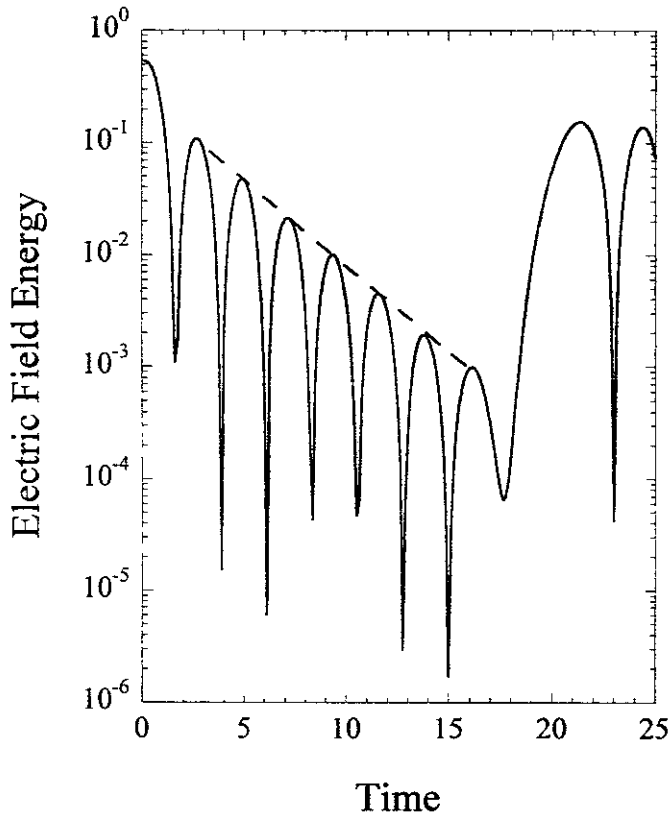

Fig.20 The full-dimensional Vlasov simulation of the Landau damping. The initial conditoin is given by $f(x,y,z,v_x,v_y,v_z,t) = (2\pi)^{-3/2}\exp(-v_x^2/2 - v_y^2/2 - v_z^2/2)(1 + A_x\cos k_x x + A_y\cos k_y y + A_z\cos k_z z)$ with $A_x = A_y = A_z = 0.01$, $k_x = k_y = k_z = 0.5$. We used M=8 mesh points in v-direction, N=8 points in x-direction and $\Delta t = 1/8$. We used an Alpha-chip based personal computer (VT-Alpha PC AXP600) and the total computational time to calculate until t=25 is 6.7 hours in CPU time. Numerical values of the damping rate and the oscillation of electric field are $\gamma = -0.176$ and $\omega = 1.4142$, respectively while the theoretical values predicted by the linear theory are $\gamma = -0.1533$ and $\omega = 1.4211$).

Recent Issues of NIFS Series

NIFS-524 T Ohkawa,
Tunneling Electron Trap; Dec 1997

NIFS-525 K Itoh, S.-I Itoh, M. Yagi, A. Fukuyama,
Solitary Radial Electric Field Structure in Tokamak Plasmas; Dec 1997

NIFS-526 Andrey N. Lyakhov,
Alfven Instabilities in FRC Plasma; Dec 1997

NIFS-527 J. Uramoto,
Net Current Increment of negative Muonlike Particle Produced by the Electron and Positive Ion Bunch-method; Dec. 1997

NIFS-528 Andrey N. Lyakhov,
Comments on Electrostastic Drift Instabilities in Field Reversed Configuraiton, Dec. 1997

NIFS-529 J. Uramoto,
Pair Creation of Negative and Positive Pionlike (Muonlike) Particle by Interaction between an Electron Bunch and a Positive Ion Bunch; Dec. 1997

NIFS-530 J. Uramoto,
Measuring Method of Decay Time of Negative Muonlike Particle by Beam Collector Applied RF Bias Voltage; Dec. 1997

NIFS-531 J. Uramoto,
Confirmation Method for Metal Plate Penetration of Low Energy Negative Pionlike or Muonlike Particle Beam under Positive Ions; Dec. 1997

NIFS-532 J Uramoto,
Pair Creations of Negative and Positive Pionlike (Muonlike) Particle or K Mesonlike (Muonlike) Particle in H2 or D2 Gas Discharge in Magnetic Field; Dec. 1997

NIFS-533 S. Kawata, C. Boonmee, T. Teramoto, L. Drska, J. Limpouch, R. Liska, M. Sinor,
Computer-Assisted Particle-in-Cell Code Development;Dec. 1997

NIFS-534 Y. Matsukawa, T. Suda, S. Ohnuki and C. Namba,
Microstructure and Mechanical Property of Neutron Irradiated TiNi Shape Memory Alloy; Jan. 1998

NIFS-535 A. Fujisawa, H. Iguchi, H. Idei, S. Kubo, K. Matsuoka, S. Okamura, K. Tanaka, T. Minami, S. Ohdachi, S. Morita, H. Zushi, S. Lee, M. Osakabe, R. Akiyama, Y. Yoshimura, K. Toi, H. Sanuki, K. Itoh, A. Shimizu, S. Takagi, A. Ejiri, C. Takahashi, M. Kojima, S. Hidekuma, K. Ida, S. Nishimura, N. Inoue, R. Sakamoto, S.-I Itoh, Y. Hamada, M. Fujiwara,
Discovery of Electric Pulsation in a Toroidal Helical Plasma; Jan. 1998

NIFS-536 Lj.R. Hadzievski, M.M. Skoric, M Kono and T. Sato,
Simulation of Weak and Strong Langmuir Collapse Regimes, Jan. 1998

NIFS-537 H. Sugama, W. Horton,
Nonlinear Electromagnetic Gyrokinetic Equation for Plasmas with Large Mean Flows, Feb. 1998

NIFS-538 H. Iguchi, T.P Crowley, A. Fujisawa, S. Lee, K Tanaka, T Minami, S. Nishimura, K. Ida, R. Akiyama, Y Hamada, H., Idei. M. Isobe, M. Kojima, S. Kubo, S. Morita, S. Ohdachi, S. Okamura, M. Osakabe, K Matsuoka, C. Takahashi and K. Toi,
Space Potential Fluctuations during MHD Activities in the Compact Helical System (CHS); Feb. 1998

NIFS-539 Takashi Yabe and Yan Zhang,
Effect of Ambient Gas on Three-Dimensional Breakup in Coronet Formation Process; Feb. 1998

NIFS-540 H. Nakamura, K. Ikeda and S. Yamaguchi,
Transport Coefficients of InSb in a Strong Magnetic Field, Feb. 1998

NIFS-541 J. Uramoto,
Development of ν_μ Beam Detector and Large Area ν_μ Beam Source by H_2 Gas Discharge (I); Mar. 1998

NIFS-542 J. Uramoto,
Development of bar{ν}$_\mu$ Beam Detector and Large Area bar{ν}$_\mu$ Beam Source by H_2 Gas Discharge (II); Mar. 1998

NIFS-543 J. Uramoto,
Some Problems inside a Mass Analyzer for Pions Extracted from a H_2 Gas Discharge; Mar. 1998

NIFS-544 J. Uramoto,
Simplified ν_μ bar{ν}$_\mu$ Beam Detector and ν_μ bar{ν}$_\mu$ Beam Source by Interaction between an Electron Bunch and a Positive Ion Bunch; Mar. 1998

NIFS-545 J. Uramoto,
Various Neutrino Beams Generated by D_2 Gas Discharge; Mar.1998

NIFS-546 R. Kanno, N Nakajima, T Hayashi and M. Okamoto,
Computational Study of Three Dimensional Equilibria with the Bootstrap Current; Mar. 1998

NIFS-547 R. Kanno, N. Nakajima and M. Okamoto,
Electron Heat Transport in a Self-Similar Structure of Magnetic Islands; Apr. 1998

NIFS-548 J.E. Rice,
Simulated Impurity Transport in LHD from MIST; May 1998

NIFS-549 M.M. Skoric, T. Sato, A.M. Maluckov and M.S. Jovanovic,
On Kinetic Complexity in a Three-Wave Interaction; June 1998

NIFS-550 S. Goto and S. Kida,
Passive Saclar Spectrum in Isotropic Turbulence: Prediction by the Lagrangian Direct-interaction Approximation; June 1998

NIFS-551 T. Kuroda, H. Sugama, R. Kanno, M. Okamoto and W. Horton,
Initial Value Problem of the Toroidal Ion Temperature Gradient Mode ; June 1998

NIFS-552 T Mutoh, R. Kumazawa, T. Seki, F. Simpo, G. Nomura, T. Ido and T. Watari,
Steady State Tests of High Voltage Ceramic Feedthoughs and Co-Axial Transmission Line of ICRF Heating System for the Large Helical Device ; June 1998

NIFS-553 N. Noda, K. Tsuzuki, A. Sagara, N. Inoue, T. Muroga,
oronaization in Future Devices -Protecting Layer against Tritium and Energetic Neutrals-: July 1998

NIFS-554 S. Murakami and H. Saleem,
Electromagnetic Effects on Rippling Instability and Tokamak Edge Fluctuations; July 1998

NIFS-555 H. Nakamura , K. Ikeda and S. Yamaguchi,
Physical Model of Nernst Element; Aug 1998

NIFS-556 H. Okumura, S. Yamaguchi, H. Nakamura, K. Ikeda and K. Sawada,
Numerical Computation of Thermoelectric and Thermomagnetic Effects, Aug. 1998

NIFS-557 Y. Takeiri, M. Osakabe, K. Tsumori, Y. Oka, O. Kaneko, E. Asano, T. Kawamoto, R. Akiyama and M. Tanaka,
Development of a High-Current Hydrogen-Negative Ion Source for LHD-NBI System; Aug.1998

NIFS-558 M. Tanaka, A. Yu Grosberg and T Tanaka,
Molecular Dynamics of Structure Organization of Polyampholytes;Sep 1998

NIFS-559 R. Horiuchi, K. Nishimura and T. Watanabe,
Kinetic Stabilization of Tilt Disruption in Field-Reversed Configurations; Sep. 1998
(IAEA-CN-69/THP1/11)

NIFS-560 S. Sudo, K. Kholopenkov, K. Matsuoka, S. Okamura, C. Takahashi, R. Akiyama, A. Fujisawa, K. Ida, H. Idei, H. Iguchi, M. Isobe, S. Kado, K. Kondo, S. Kubo, H. Kuramoto, T. Minami, S. Morita, S. Nishimura, M. Osakabe, M. Sasao, B Peterson, K. Tanaka, K, Toi and Y. Yoshimura,
Particle Transport Study with Tracer-Encapsulated Solid Pellet Injection;Oct. 1998
(IAEA-CN-69/EXP1/18)

NIFS-561 A. Fujisawa, H. Iguchi, S Lee, K. Tanaka, T. Minami, Y. Yoshimura, M. Osakabe, K. Matsuoka, S. Okamura, H Idei, S. Kubo, S. Ohdachi, S. Morita, R. Akiyama, K. Toi, H. Sanuki, K. Itoh, K Ida, A. Shimizu, S. Takagi, C. Takahashi, M. Kojima, S. Hidekuma, S Nishimura, M. Isobe, A. Ejiri, N Inoue, R Sakamoto, Y Hamada and M Fujiwara,
Dynamic Behavior Associated with Electric Field Transitions in CHS Heliotron/Torsatron; Oct 1998
(IAEA-CN-69/EX5/1)

NIFS-562 S. Yoshikawa,
Next Generation Toroidal Devices; Oct 1998

NIFS-563 Y. Todo and T. Sato,
Kinetic-Magnetohydrodynamic Simulation Study of Fast Ions and Toroidal Alfvén Eigenmodes; Oct 1998
(IAEA-CN-69/THP2/22)

NIFS-564 T Watari, T. Shimozuma, Y Takeiri, R Kumazawa, T. Mutoh, M. Sato, O. Kaneko, K. Ohkubo, S. Kubo, H Idei, Y Oka, M. Osakabe, T. Seki, K. Tsumori, Y. Yoshimura, R. Akiyama, T Kawamoto, S. Kobayashi, F. Shimpo, Y Takita, E Asano, S Itoh, G Nomura, T. Ido, M. Hamabe, M. Fujiwara, A Iiyoshi, S. Morimoto, T Bigelow and Y.P. Zhao,
Steady State Heating Technology Development for LHD; Oct. 1998
(IAEA-CN-69/FTP/21)

NIFS-565 A. Sagara, K.Y. Watanabe, K. Yamazaki, O. Motojima, M. Fujiwara, O. Mitarai, S. Imagawa, H. Yamanishi, H Chikaraishi, A Kohyama, H. Matsui, T Muroga, T. Noda, N Ohyabu, T. Satow, A.A. Shishkin, S. Tanaka, T. Terai and T. Uda,
LHD-Type Compact Helical Reactors; Oct 1998
(IAEA-CN-69/FTP/03(R)

NIFS-566 N. Nakajima, J. Chen, K. Ichiguchi and M. Okamoto,
Global Mode Analysis of Ideal MHD Modes in L=2 Heliotron/Torsatron Systems; Oct 1998
(IAEA-CN-69/THP1/08)

NIFS-567 K Ida, M Osakabe, K. Tanaka, T Minami, S. Nishimura, S Okamura, A. Fujisawa, Y. Yoshimura, S Kubo, R. Akiyama, D.S.Darrow, H. Idei, H. Iguchi, M. Isobe, S. Kado, T. Kondo, S Lee, K Matsuoka, S. Morita, I. Nomura, S. Ohdachi, M. Sasao, A. Shimizu, K. Tumori, S. Takayama, M Takechi, S Takagi, C Takahashi, K. Toi and T. Watari,
Transition from L Mode to High Ion Temperature Mode in CHS Heliotron/Torsatron Plasmas; Oct. 1998
(IAEA-CN-69/EX2/2)

NIFS-568 S. Okamura, K. Matsuoka, R. Akiyama, D.S. Darrow, A. Ejiri, A. Fujisawa, M. Fujiwara, M. Goto, K. Ida H. Idei, H. Iguchi, N. Inoue, M. Isobe, K. Itoh, S. Kado, K. Khlopenkov, T. Kondo, S. Kubo, A Lazaros, S. Lee, G. Matsunaga, T. Minami, S Morita, S Murakami, N. Nakajima, N. Nikai, S. Nishimura, I Nomura, S. Ohdachi, K. Ohkuni, M. Osakabe, R. Pavlichenko, B. Peterson, R. Sakamoto, H. Sanuki, M. Sasao, A. Shimizu, Y. Shirai, S. Sudo, S. Takagi, C. Takahashi, S. Takayama, M. Takechi, K. Tanaka, K. Toi, K. Yamazaki, Y. Yoshimura and T. Watari,
Confinement Physics Study in a Small Low-Aspect-Ratio Helical Device CHS; Oct. 1998
(IAEA-CN-69/OV4/5)

NIFS-569 M.M. Skoric, T. Sato, A. Maluckov, M.S. Jovanovic,
Micro- and Macro-scale Self-organization in a Dissipative Plasma. Oct 1998

NIFS-570 T. Hayashi, N. Mizuguchi, T-H. Watanabe, T. Sato and the Complexity Simulation Group,
Nonlinear Simulations of Internal Reconnection Event in Spherical Tokamak; Oct 1998
(IAEA-CN-69/TH3/3)

NIFS-571 A. Iiyoshi, A. Komori, A. Ejiri, M. Emoto, H Funaba, M. Goto, K. Ida, H. Idei, S Inagaki, S. Kado, O Kaneko, K. Kawahata, S. Kubo, R. Kumazawa, S Masuzaki, T. Minami, J. Miyazawa, T. Morisaki, S. Morita, S. Murakami, S Muto, T Muto, Y. Nagayama, Y. Nakamura, H. Nakanishi, K. Narihara, K. Nishimura, N. Noda, T. Kobuchi, S. Ohdachi, N. Ohyabu, Y. Oka, M. Osakabe, T. Ozaki, B.J. Peterson, A. Sagara, S Sakakibara, R. Sakamoto, H. Sasao, M. Sasao, K. Sato, M. Sato, T. Seki, T. Shimozuma, M. Shoji, H. Suzuki, Y. Takeiri, K Tanaka, K. Toi, T. Tokuzawa, K Tsumori, I. Yamada, H. Yamada, S. Yamaguchi, M Yokoyama, K.Y.Watanabe, T. Watari, R Akiyama, H. Chikaraishi, K. Haba, S. Hamaguchi, S. Iima, S. Imagawa, N. Inoue, K Iwamoto, S. Kitagawa, Y. Kubota, J Kodaira, R. Maekawa, T. Mito T. Nagasaka, A. Nishimura, Y Takita, C Takahashi, K. Takahata, K. Yamauchi, H. Tamura, T. Tsuzuki, S. Yamada, N. Yanagi, H. Yonezu, Y. Hamada, K Matsuoka, K. Murai, K. Ohkubo, I. Ohtake, M. Okamoto, S. Sato, T. Satow, S. Sudo, S. Tanahashi, K. Yamazaki, M. Fujiwara and O. Motojima,
An Overview of the Large Helical Device Project; Oct. 1998
(IAEA-CN-69/OV1/4)

NIFS-572 M. Fujiwara, H Yamada, A. Ejiri, M. Emoto, H. Funaba, M. Goto, K. Ida, H Idei, S. Inagaki, S Kado, O. Kaneko, K. Kawahata, A. Komori, S. Kubo, R. Kumazawa, S. Masuzaki, T Minami, J. Miyazawa, T. Morisaki, S. Morita, S. Murakami, S. Muto, T. Muto, Y Nagayama, Y Nakamura, H. Nakanishi, K. Narihara, K Nishimura, N. Noda, T. Kobuchi, S. Ohdachi, N. Ohyabu, Y. Oka, M. Osakabe, T. Ozaki, B. J. Peterson, A. Sagara, S. Sakakibara, R. Sakamoto, H. Sasao, M. Sasao, K. Sato, M. Sato, T. Seki, T. Shimozuma, M. Shoji, H. Sazuki, Y. Takeiri, K Tanaka, K. Toi, T. Tokuzawa, K. Tsumori, I. Yamada, S Yamaguchi, M. Yokoyama, K.Y. Watanabe, T. Watari, R. Akiyama, H. Chikaraishi, K. Haba, S. Hamaguchi, M. Iima, S. Imagawa, N. Inoue, K. Iwamoto, S. Kitagawa, Y Kubota, J Kodaira, R Maekawa, T Mito, T. Nagasaka, A. Nishimura, Y. Takita, C. Takahashi, K. Takahata, K. Yamauchi, H. Tamura, T. Tsuzuki, S. Yamada, N. Yanagi, H. Yonezu, Y. Hamada, K. Matsuoka, K. Murai, K. Ohkubo, I. Ohtake, M Okamoto, S. Sato, T. Satow, S. Sudo, S. Tanahashi, K Yamazaki, O Motojima and A. Iiyoshi,
Plasma Confinement Studies in LHD; Oct 1998
(IAEA-CN-69/EX2/3)

NIFS-573 O. Motojima, K. Akaishi, H. Chikaraishi, H. Funaba, S. Hamaguchi, S. Imagawa, S. Inagaki, N. Inoue, A. Iwamoto, S. Kitagawa, A. Komori, Y. Kubota, R. Maekawa, S. Masuzaki, T. Mito, J. Miyazawa, T. Morisaki, T. Muroga, T. Nagasaka, Y. Nakmura, A. Nishimura, K. Nishimura, N. Noda, N. Ohyabu, S. Sagara, S. Sakakibara, R. Sakamoto, S. Satoh, T Satow, M. Shoji, H. Suzuki, K. Takahata, H. Tamura, K. Watanabe, H. Yamada, S. Yamada, S. Yamaguchi, K. Yamazaki, N. Yanagi, T. Baba, H. Hayashi, M. Iima, T. Inoue, S. Kato, T. Kato, T Kondo, S. Moriuchi, H. Ogawa, I. Ohtake, K. Ooba, H. Sekiguchi, N. Suzuki, S. Takami, Y. Taniguchi, T. Tsuzuki, N. Yamamoto, K. Yasui, H. Yonezu, M. Fujiwara and A. Iiyoshi,
Progress Summary of LHD Engineering Design and Construction; Oct. 1998
(IAEA-CN-69/FT2/1)

NIFS-574 K. Toi, M. Takechi, S. Takagi, G. Matsunaga, M. Isobe, T Kondo, M. Sasao, D.S. Darrow, K. Ohkuni, S. Ohdachi, R Akiyama A. Fujisawa, M. Gotoh, H. Idei, K. Ida, H. Iguchi, S. Kado, M. Kojima, S. Kubo, S. Lee, K. Matsuoka, T. Minami, S. Morita, N. Nikai, S. Nishimura, S. Okamura, M. Osakabe, A. Shimizu, Y. Shirai, C. Takahashi, K. Tanaka, T. Watari and Y. Yoshimura,
Global MHD Modes Excited by Energetic Ions in Heliotron/Torsatron Plasmas;Oct. 1998
(IAEA-CN-69/EXP1/19)

NIFS-575 Y Hamada, A. Nishizawa, Y. Kawasumi, A. Fujisawa, M. Kojima, K. Narihara, K. Ida, A. Ejiri, S. Ohdachi, K. Kawahata, K. Toi, K. Sato, T. Seki, H. Iguchi, K. Adachi, S. Hidekuma, S.Hirokura, K. Iwasaki, T Ido, R. Kumazawa, H. Kuramoto, T Minami, I. Nomura, M. Sasao, K.N. Sato, T. Tsuzuki, I. Yamada and T. Watari,
Potential Turbulence in Tokamak Plasmas;Oct. 1998
(IAEA-CN-69/EXP2/14)

NIFS-576 S. Murakami, U. Gasparino, H. Idei, S. Kubo, H. Maassberg, N. Marushchenko, N. Nakajima, M. Romé and M. Okamoto,
5D Simulation Study of Suprathermal Electron Transport in Non-Axisymmetric Plasmas;Oct. 1998
(IAEA-CN-69/THP1/01)

NIFS-577 S. Fujiwara and T. Sato,
Molecular Dynamics Simulation of Structure Formation of Short Chain Molecules; Nov. 1998

NIFS-578 T. Yamagishi,
Eigenfunctions for Vlasov Equation in Multi-species Plasmas Nov. 1998

NIFS-579 M. Tanaka, A. Yu Grosberg and T. Tanaka,
Molecular Dynamics of Strongly-Coupled Multichain Coulomb Polymers in Pure and Salt Aqueous Solutions;Nov. 1998

NIFS-580 J. Chen, N. Nakajima and M. Okamoto,
Global Mode Analysis of Ideal MHD Modes in a Heliotron/Torsatron System: I. Mercier-unstable Equilibria;Dec. 1998

NIFS-581 M. Tanaka, A. Yu Grosberg and T. Tanaka,
Comparison of Multichain Coulomb Polymers in Isolated and Periodic Systems: Molecular Dynamics Study; Jan. 1999

NIFS-582 V.S. Chan and S. Murakami,
Self-Consistent Electric Field Effect on Electron Transport of ECH Plasmas; Feb. 1999

NIFS-583 M. Yokoyama, N. Nakajima, M. Okamoto, Y. Nakamura and M. Wakatani,
Roles of Bumpy Field on Collisionless Particle Confinement in Helical-Axis Heliotrons;Feb. 1999

NIFS-584 T.-H. Watanabe, T. Hayashi, T. Sato, M. Yamada and H. Ji,
Modeling of Magnetic Island Formation in Magnetic Reconnection Experiment;Feb 1999

NIFS-585 R. Kumazawa, T. Mutoh, T. Seki, F Shinpo, G. Nomura, T. Ido, T. Watari, Jean-Marie Noterdaeme and Yangping Zhao,
Liquid Stub Tuner for Ion Cyclotron Heating;Mar. 1999

NIFS-586 A. Sagara, M. Iima, S. Inagaki, N. Inoue, H. Suzuki, K. Tsuzuki, S. Masuzaki, J. Miyazawa, S. Morita, Y. Nakamura, N. Noda, B. Peterson, S. Sakakibara, T Shimozuma, H Yamada, K. Akaishi, H. Chikaraishi, H. Funaba, O Kaneko, K. Kawahata, A. Komori, N. Ohyabu, O. Motojima, LHD Exp. Group 1, LHD Exp. Group 2,
Wall Conditioning at the Starting Phase of LHD;Mar. 1999

NIFS-587 T. Nakamura and T. Yabe,
Cubic Interpolated Propagation Scheme for Solving the Hyper-Dimensional Vlasov-Poisson Equation in Phase Space;Mar. 1999